

Supplementary Information

Delocalized C=S decorates 3D sp^2 -hybridized carbon skeleton for superior charge transfer kinetics of anodes

Fei Wang,^{ab} Zhendong Liu,^b Zhijie Xiang,^a Chengzhi Zhang,^{*b} Anbang Lu,^b Fulai Qi,^c Jun Tan,^{*b} and Jinshui Liu^{*a}

^a Hunan Province Key Laboratory for Advanced Carbon Materials and Applied Technology, College of Materials Science and Engineering, Hunan University, Changsha, Hunan, 410082, China

^b Ji Hua Laboratory, Foshan, Guangdong, 528000, China

^c Institute of Science and Technology for New Energy, Xi'an Technological University, Xi'an, Shanxi, 710021, China

* Email: zhangchz@jihualab.ac.cn, tanjun@jihualab.ac.cn, Jsliu@hnu.edu.cn

Experimental Section

First, dopamine is self-polymerized in Tris-HCl solution (PH = 8.5), resulting in poly-dopamine (PDA) that is uniformly coated on the surface of polystyrene spheres (PS) nanoparticles for 24 h, thereby forming PDA@PS precursor. The ratio of dopamine and PS is 1:2 (*wt./wt.*). Second, the precursor is calcined under Ar atmosphere with under the heat preservation temperature of 500 °C and a heating rate of 2 °C min⁻¹. During the calcination process, PDA and PS were simultaneously carbonized into five-membered-ring N-rich hollow carbon spheres (C4N/HCSs), which causes mesopores on the carbon wall. The C4S/HCSs is obtained by treating C4N/HCSs under Ar/CS₂-mixed atmosphere (0.05 L min⁻¹) at 550 °C for 4 hours with a heating rate of 2 °C min⁻¹. Similarly, the C4S/HCSs are obtained by treating C4N/HCSs under Ar/H₂S-mixed atmosphere (0.05 L min⁻¹) at 550 °C for 4 hours with a heating rate of 2 °C min⁻¹. The C4S-S/HCSs are obtained by mixing C4N/HCSs and sulfur powder with 1:5 *wt./wt.* under Ar atmosphere (0.05 L min⁻¹) at 550 °C for 4 hours with a heating rate of 2 °C min⁻¹, and then purging the residual sulfur powder on the surface of material with a high Ar flow rate (0.2 L min⁻¹) for 1 hours.

Material characterization

The morphology of samples was recorded by a field-emission scanning electron microscopy (SEM, Verios G4 UC). A scanning transmission electron microscope with image corrector (HRTEM, FEI Tecnai G2 F20) was utilized to obtain transmission electron microscopy (TEM) images and high-resolution TEM (HRTEM) images, as well as energy-dispersive X-ray spectroscopy (EDX). The surface chemical compositions of the prepared materials were characterized by an X-ray photoelectron spectroscopy (XPS, ESCALAB 250 instrument with Al K α radiation (15 kV, 150 W) under a pressure of 4×10^{-8} Pa). The crystal structure was carried out by a powder X-ray diffraction (XRD, Bruker D2 Advance diffractometer, Rigaku diffractometer using Cu K α radiation). Thermal gravimetric analysis (TGA) was examined by Shimadzu DTG-60 thermal analyzer at a heating rate of 10 °C min⁻¹ under an air atmosphere. The Raman spectra were investigated on a confocal Raman spectrometer (WITec Alpha-300R, 532 nm). FTIR spectra were obtained using a Nicolet iS5 iD7 spectrometer in Ar atmosphere. A time-of-flight secondary ion mass spectrometer (TOF-SIMS 5, ION-TOF) at a pressure below 10^{-9} , negative mode was used to analyse the chemical bonding structure of the as-prepared composites film. The specific surface area was calculated by the Brunauer-Emmett-Teller theory and the pore size distribution was calculated by a density functional theory method (Micromeritics ASAP 2020HD instrument) at liquid-nitrogen temperature based on Brunauer-Emmett-Teller (BET) model. The elemental analysis (EA) was

measured by a Vario Macro Cube elemental analyzer (Elementar) with Model-CHNS for determining carbon (C), hydrogen(H), nitrogen (N) and sulfur (S) content, and with Model-O for measuring oxygen (O) content. The carbon vacancy structure was tested by electron paramagnetic resonance (EPR, Bruker EMXPLUS). The ST-2722 Semiconductor resistivity of the powder tester was employed to measure the powder electronic conductivity (σ_a) of samples.

Electrochemical Measurements

All electrochemical tests were conducted by using 2025-type button half-cells in an Ar-filled glovebox. To fabricate working electrodes, active material, conductive carbon black and sodium alginate (SA) at a weight ratio of 8:1:1 were dispersed in mixed ethanol/water solvent to form a well-proportioned electrode slurry mixture. The slurry was then spread on Cu foil and then dried at 80 °C overnight (12 hours) in a vacuum oven. The mass loading of as-prepared wafer was found to be 1.2-1.5 mg cm⁻² with a diameter of 12 mm. PE separator (16 μm) in LIBs and glass fiber (GF/D, Whatman) in KIBs and SIBs were used as separator. The electrolyte consists of 1.0 M lithium hexafluorophosphate (LiPF₆) in 1:1 (wt./wt.) ethylene carbonate (EC)/diethylene carbonate (DEC), 1.0 M sodium hexafluorophosphate (NaPF₆) in 1:1 (wt./wt.) EC/DEC, 0.8 M potassium hexafluorophosphate (KPF₆) in 1:1 (wt./wt.) EC/DEC. And 200 μL of the electrolyte was injected to each cell tested. The galvanostatic cycle tests of half-cells and GITT were conducted in Land CT2001A battery testing system with a wide window of 0.005-3 V at 25 °C. Before testing, cells were under rest for 8 h to ensure sufficient soaking of the electrolyte into the separator and electrodes. For *Ex-situ* measurements of the electrodes after cycling, the electrodes were cleaned by DEC to remove any residual alkali metal salts from the surface of the electrodes. The electrochemical impedance spectroscopy measurements were performed using a potentiostat (VSP, Bio-Logic) over frequency range from 100 MHz to 0.1 Hz. CV analysis was conducted for kinetic study at a series of scan rates (0.1, 0.2, 0.3, 0.5, 1.0, 2.0, and 5.0 mV s⁻¹) in the potential range of 0.005-3.0 V. *In-situ* XRD performance (XRD Bruker D2 Phaser diffractometer) of C5=S/HCSs and C4S-S/HCSs electrodes (without conductive carbon black, a weight ratio of active material and binder is 9:1) were cycled at 0.005-3.0 V at 0.2 A g⁻¹ with a Land CT2001A battery test system. *In-suit* cell: Beijing Scistar Technology Co. Ltd.

Computational Methods

The simulation calculations in this work were based on the density functional theory (DFT) with the gradient exchange-correlation functional of Perdew-Burke-Ernzerhof (PBE)

functional. In order to consider effect of electrostatic interactions between molecules or atoms on the structure, the calculations applied DFT-D3 method. In the expansion of the plane wave, the used kinetic cutoff energy was 450 eV. Optimization algorithm for wave functions two electron iterative algorithms were applied. Conjugate gradient algorithm was used for geometric optimization until the force on all unconstrained atoms was less than 0.03 eV Å⁻¹. To prevent artificial electrostatic fields, a dipole correction was applied in the surface normal direction to calculate all the energies reported here.

Through the lattice structure information of the stable system, the Schrödinger equation is further solved through self-consistent iterative, and the Fermi energy level, wave function of electrons, charge density and other information under the ground state of the system are completely calculated, and then the bonding between atoms is directly analyzed, functional with the plane-wave-cut-off energy of 450 eV, a set of $5 \times 5 \times 5$ k-points, and the threshold of self-consistent-field energy convergence of 10^{-6} eV.

The calculation formula of difference charge density: $\Delta\rho = \rho_{AB} - \rho_A - \rho_B$. ρ_{AB} represents the optimized structural charge density of the interface, ρ_A represents the charge density of the material A making up the interface, and ρ_B represents the charge density of the material B making up the interface. By subtraction, the change of charge density after the interface AB formed by materials A and B can be obtained, and then the properties such as charge movement in the interface can be analyzed. In this study: A indicates C5=S/HCSs, C4S-S/HCSs or C4S/HCSs, and B indicates K atom.

Doping effects of S atom in carbon skeleton were investigated based on atomic net charge distribution analysis by using the Bader method in which charge transfer in DFT calculations is quantified by the net atomic charges. Our Bader analysis for S, and C is obtained from charge density generated by first-principles DFT calculations. The crystal orbital Hamiltonian layout (COHP) was obtained from the self-consistent wave function by analyzing the local auxiliary

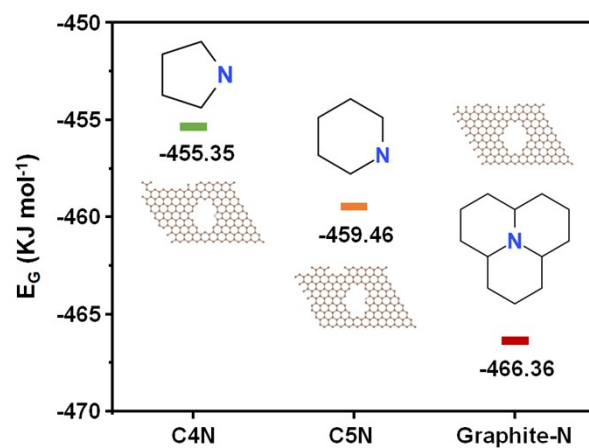
base set projected onto valence s and p orbitals by Lobster software (<http://www.cohp.de>). The wave function was calculated through the projector-augmented wave method by VASP. This calculation depends on the basis function chosen in the later LOBSTER run. LOBSTER then projects this wave function onto a basis set of atomic orbitals that must be adapted to the system at hand, corresponding to a unitary transformation between a totally delocalized and a localized representation.

In this work, the CI-NEB method was used to search for the transition state, increase the calculation accuracy of the force on the basis of structural relaxation to $1\text{E-}7$, enable the optimization algorithm that comes with VASP, and carry out interpolation points at 4 positions. To verify the transition state, we verified the frequency and found that it has only one imaginary frequency.

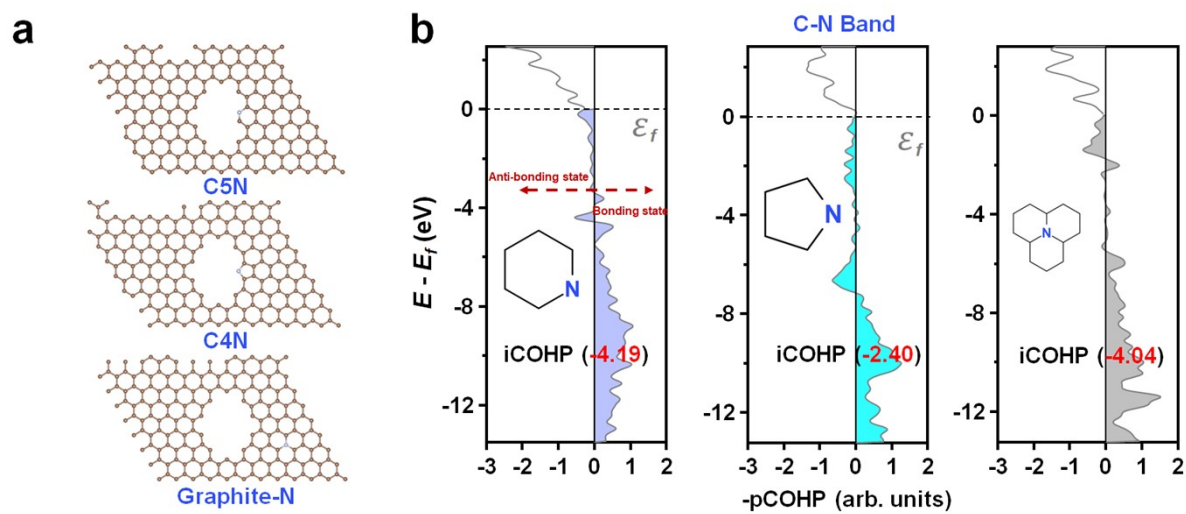
Supplementary Equations

$\sigma = \frac{1}{3} e^2 V_F^2 \tau g(E_F)$	Equation S1
$D = \frac{R^2 T^2}{2 A^2 n^4 F^4 C^2 \sigma^2}$	Equation S2
$Z_{real} = R_e + R_{ct} + \sigma \omega^{-1/2}$	Equation S3
$k = A e^{-\frac{E_a}{RT}}$ $\frac{d \ln k}{dT} = \frac{E_a}{RT^2}$ $E_a = RT^2 \frac{d \ln k}{dT} = -R \frac{d \ln k}{d \frac{1}{T}}$	Equation S4
$\dot{i} = a v^b$	Equation S5
$\log(i) = b \log(v) + \log(a)$	Equation S6
$\ddot{i} = k_1 v + k_2 v^{1/2}$	Equation S7
$D = \frac{4}{\pi \tau} \left\{ \frac{m_B V_m}{M_B A} \right\}^2 \left(\frac{\Delta E_s}{\Delta E_\tau} \right)^2$	Equation S8
$\rho = \frac{1}{V_{total} + \frac{1}{\rho_{carbon}}}$	Equation S9

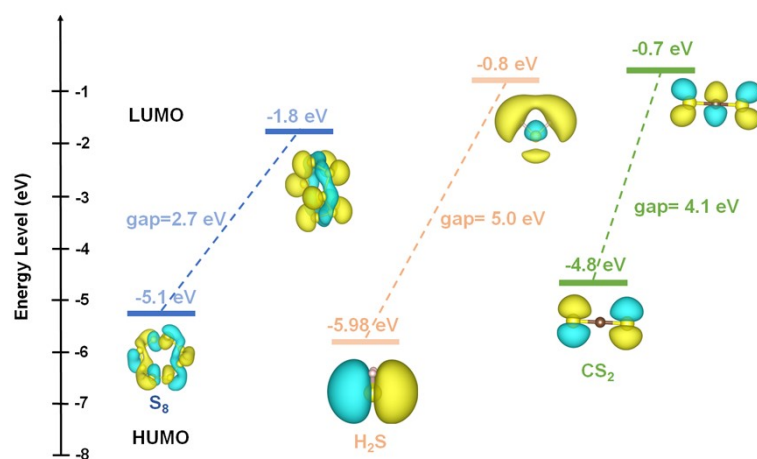
Supplementary Figures



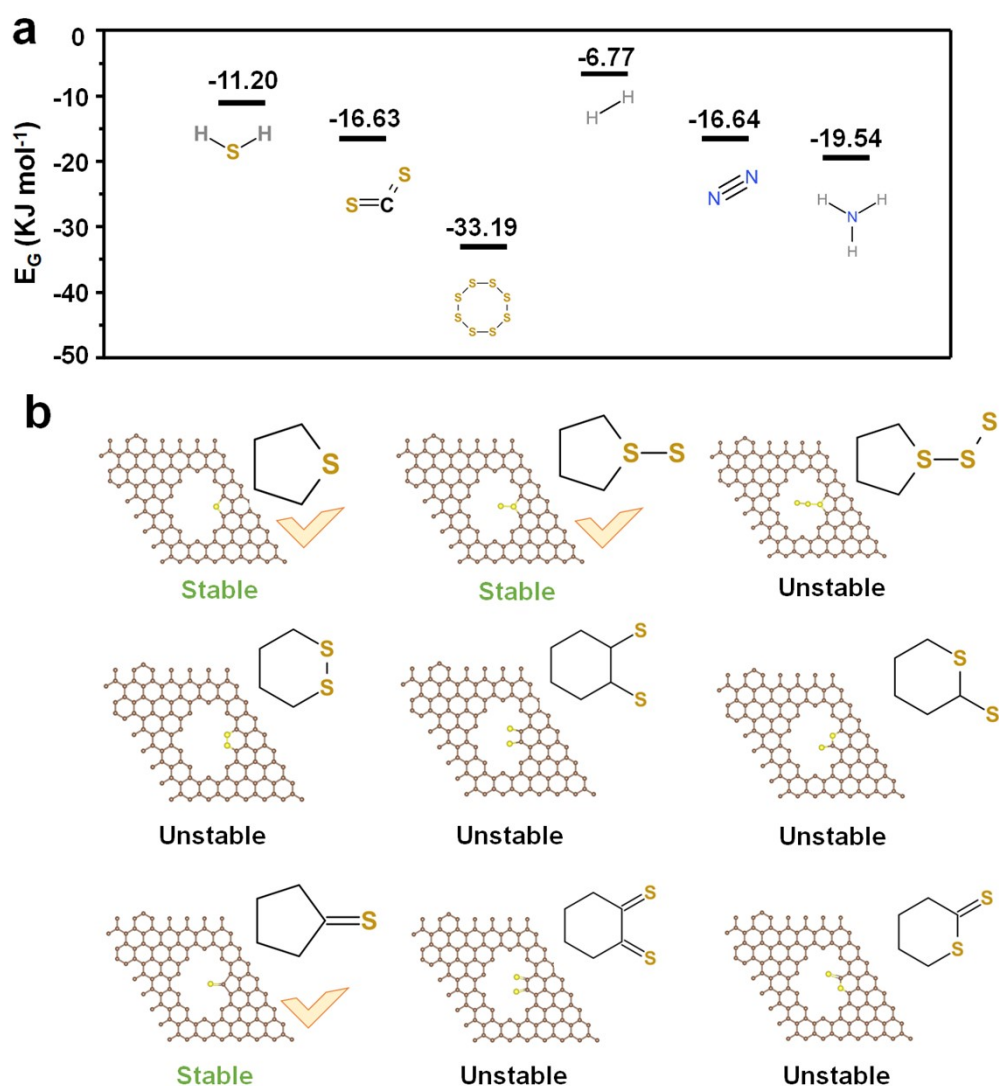
Supplementary Fig. 1. The Gibbs free enthalpy of graphene layer with pyridine-N (six-membered-ring N, C5N), pyrrole-N (five-membered-ring N, C4N), and Graphite-N.



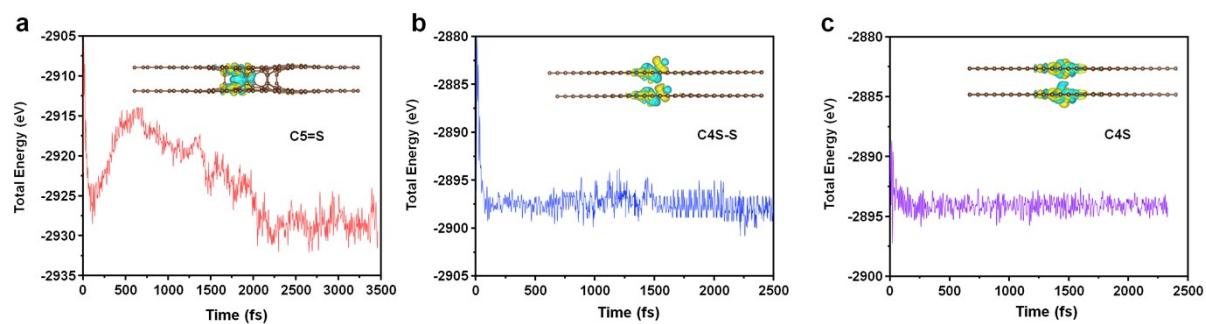
Supplementary Fig. 2. The models of graphene with six-membered-ring N (C5N) and five-membered-ring N (C4N). (b) COHP analysis of the C5N and C4N models, and the integration value of $-i\text{COHP}$ value was used to compare the bonding strength of C-N bond.



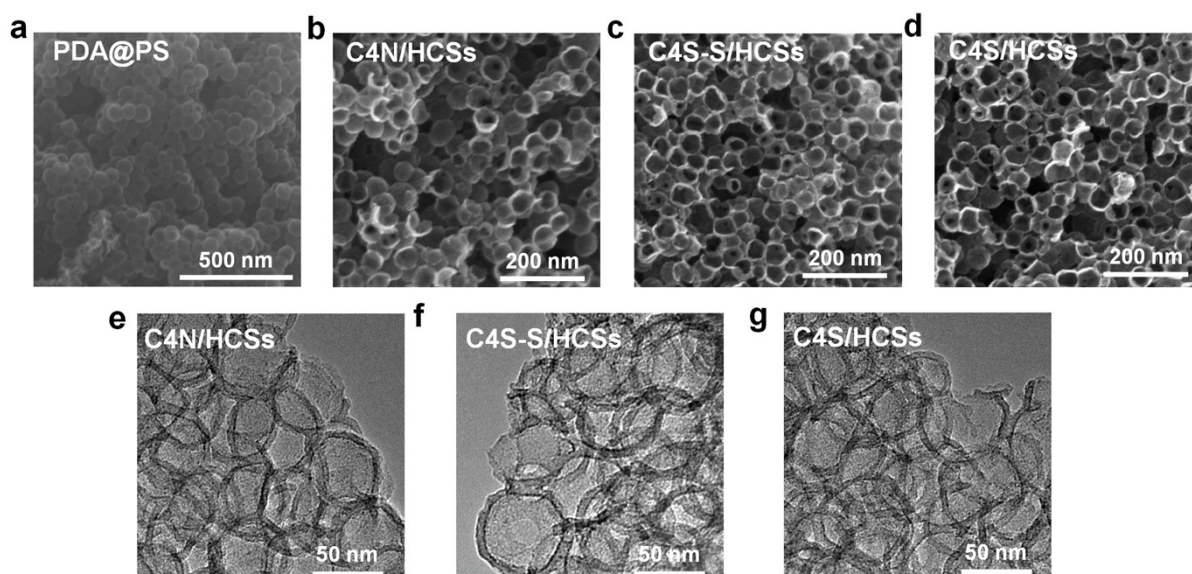
Supplementary Fig. 3. The values of HOMO and LUMO energy level of different S dopants sources (CS₂, H₂S and CS₂) in this work.



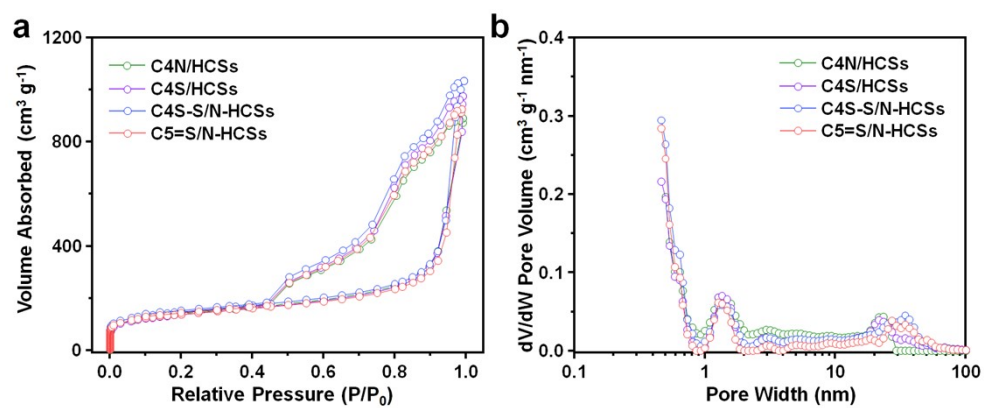
Supplementary Fig. 4. Simulation analysis of the reaction mechanism: (a) The Gibbs free enthalpy of different molecules in the functional bonds grafting conversion. (b) Three stable structural models selected through computational simulation.



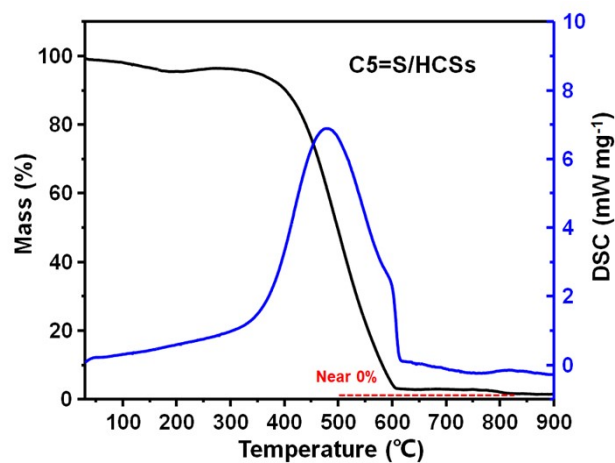
Supplementary Fig. 5. Thermodynamic enthalpy simulation of three C/S bond doped carbon skeleton at 823.15 K, corresponding to the Supplementary Video. 1-3.



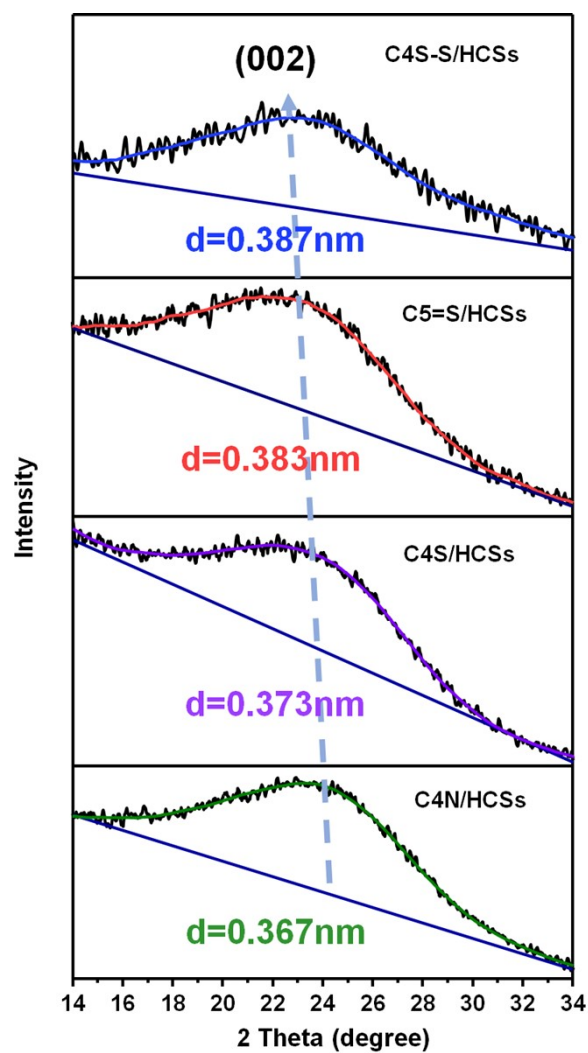
Supplementary Fig. 6. The SEM images of the composites called (a) PDA@PS in the field of 500 nm, and composites named (b) C4N/HCSs, (c) C4S-S/HCSs and (d) C4S/HCSs in the field of 200 nm. And TEM images of (e) C4N/HCSs, (f) C4S-S/HCSs and (g) C4S/HCSs composites in the field of 50 nm.



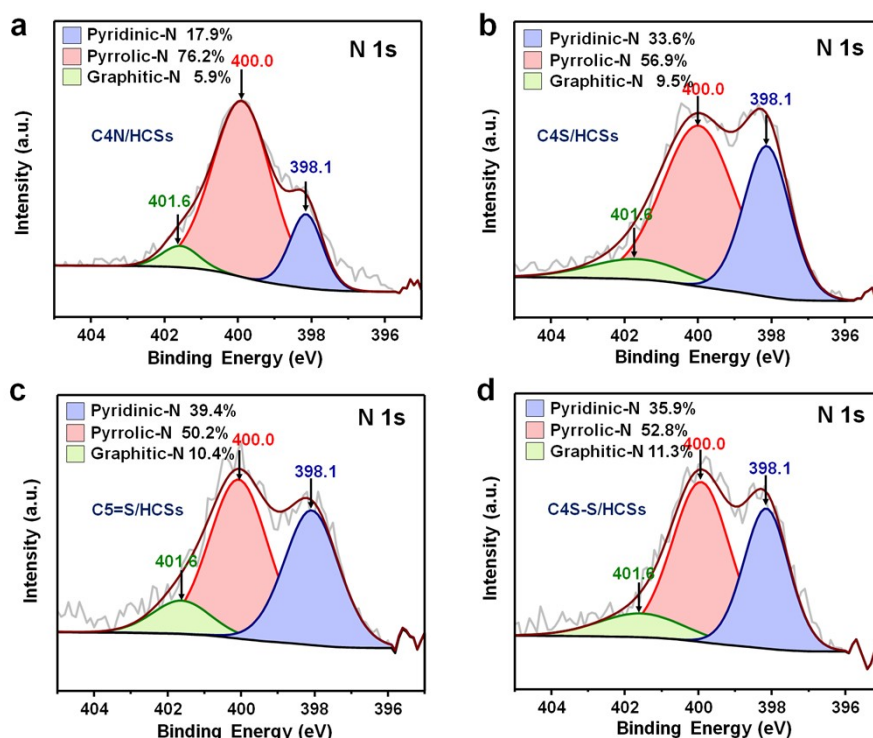
Supplementary Fig. 7. (a) The N₂ adsorption/desorption isotherms with the corresponding. (b) PSD curves of CNS with BJH pore distribution.



Supplementary Fig. 8. Thermogravimetric analysis curve of C5=S/HCSs in air atmosphere with a heating rate of 5 °C min⁻¹.



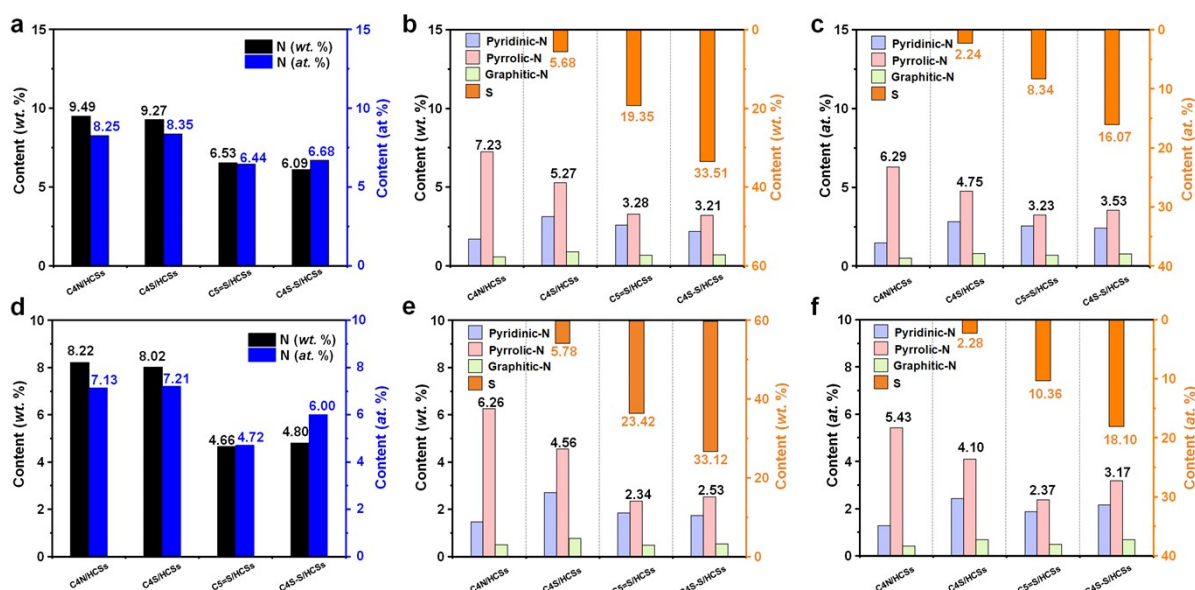
Supplementary Fig. 9. The influence of different C-S bonds on the interlayer spacing: wide-angle X-ray diffraction patterns of the C5=S/HCSs, C4S-S/HCSs, C4S/HCSs, and C4N/HCSs.



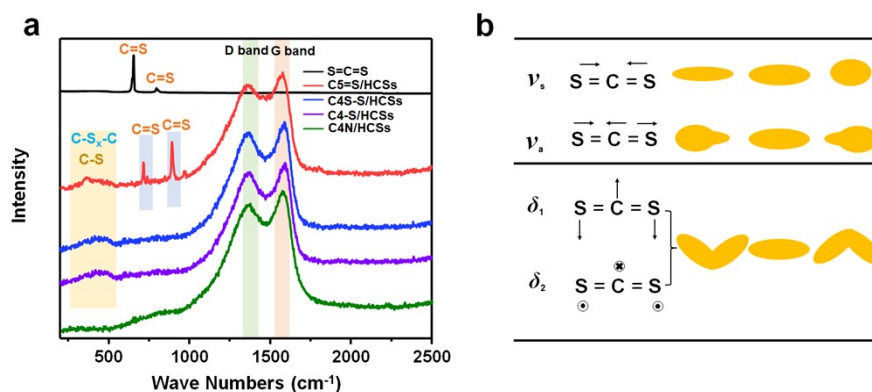
Supplementary Fig. 10. The XPS N 1s high resolution-spectra of (a) C4N/HCSs, (b) C4S/HCSs, (c) C5=S/HCSs and (d) C4S-S/HCSs. It fitted into three distinct peaks, represent pyridinic N, graphite N, and pyrrolic N.

Note: There are two main reaction pathways in the mechanism of dopamine polymerization, namely BINAP ring and Michael ring. BINAP rings are cyclic products composed of nitrogen-containing double bonds, which contain dopamine catalysts, which can effectively promote the reaction and produce the corresponding five-membered-ring product. The value of PH and the concentration, temperature, time of polymerization could be precisely controlling the generation of BINAP rings. After carbonization, the formation of the C4N structure would be achieved.

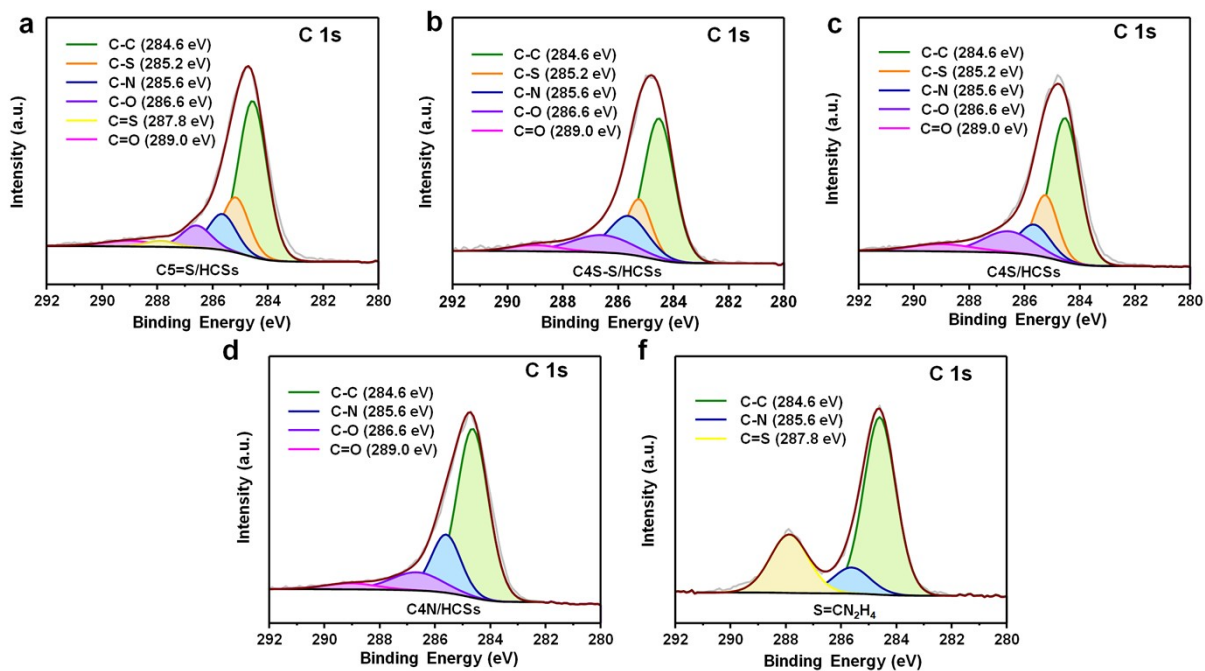
The C4N/HCSs is the precursor, and some N atoms will be replaced by S after sulfuration, especially pyrrole nitrogen, so the content of pyrrole nitrogen in C4N/HCSs will be greatly reduced, while the content of pyridine nitrogen and graphite nitrogen will increase approximately in equal proportion.



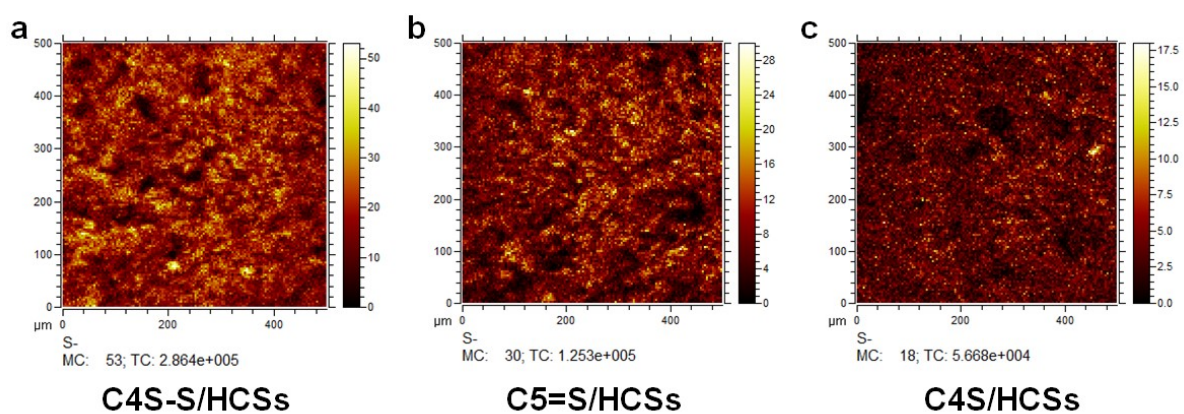
Supplementary Fig. 11. (a) The XPS N elemental contents (wt.% and at.%) of C4N/HCSs, C4S/HCSs, C5=S/HCSs, and C4S-S/HCSs. (b-c) Statistical chart of elemental contents evolution after three different S bonds grafted (b) wt.% (c) at.%. (d) The elemental analysis result of C4N/HCSs, C4S/HCSs, C5=S/HCSs, and C4S-S/HCSs. (e-f) Statistical chart of elemental contents evolution after three different S bonds grafted (e) wt.% (f) at.%.









Supplementary Fig. 12. The Raman spectra of liquid S=C=S in different compounds. (a) The characteristic signals of C=S bonds. (b) The antisymmetric stretching vibration and symmetrical stretching vibration model of C=S bonds.



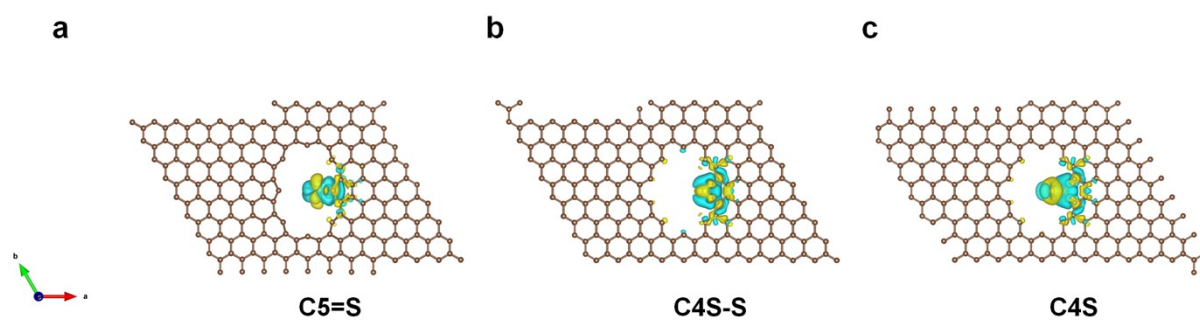
Supplementary Fig. 13. The XPS C 1s high resolution spectra of (a) C5=S/HCSs is fitted into six distinct peaks. Correspondingly, (b) C4S-S/HCSs, (c) C4S/HCSs is five distinct peaks, (d) C4N/HCSs is four distinct peaks and (e) S=CN₂H₄ is three distinct peaks.



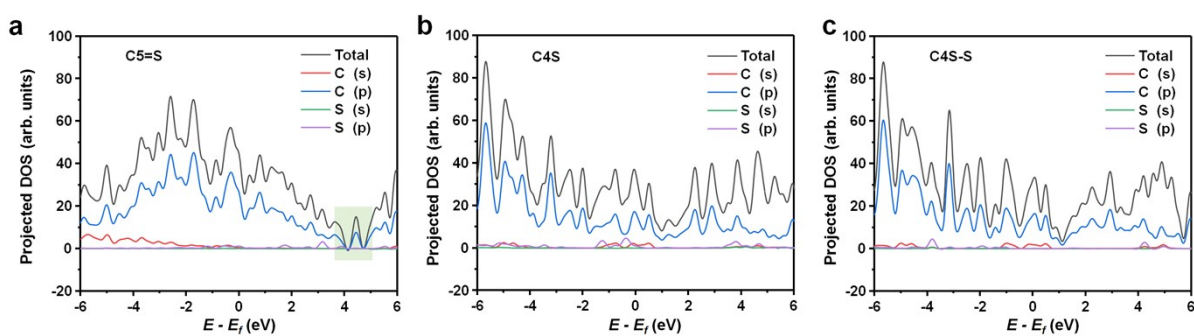
Supplementary Fig. 14. The secondary ion imaging mapping of (a) C4S-S/HCSs, (b) C5=S/HCSs and (c) C4S/HCSs.

	C4S-S/HCSs	C5=S/HCSs	C4S/NCSs
C=S			
C-S-C			
C-S-S	 Many		 Little

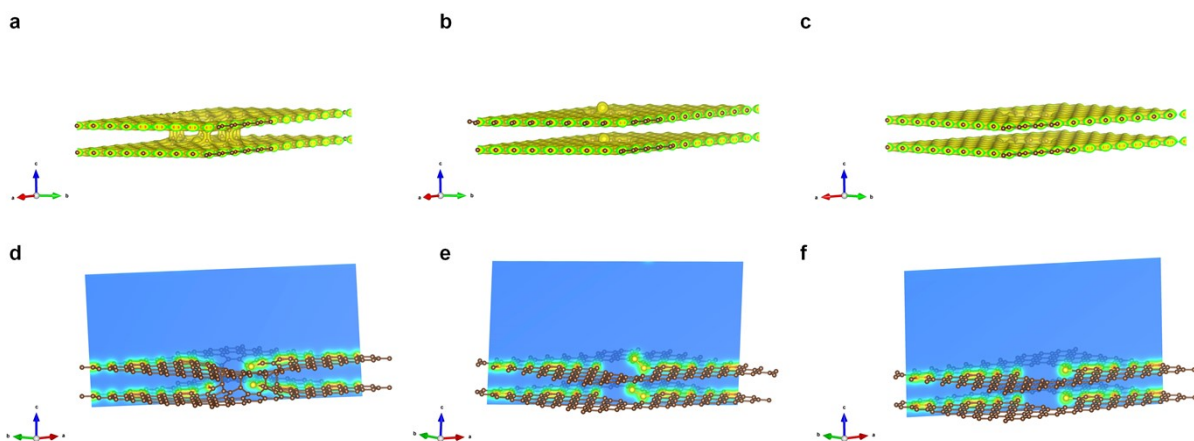
Supplementary Fig. 15. The statistical chart of evaluated bonding structure between C and S in terms of C5=S/HCSs, C4S-S/HCSs, and C4S/HCSs.



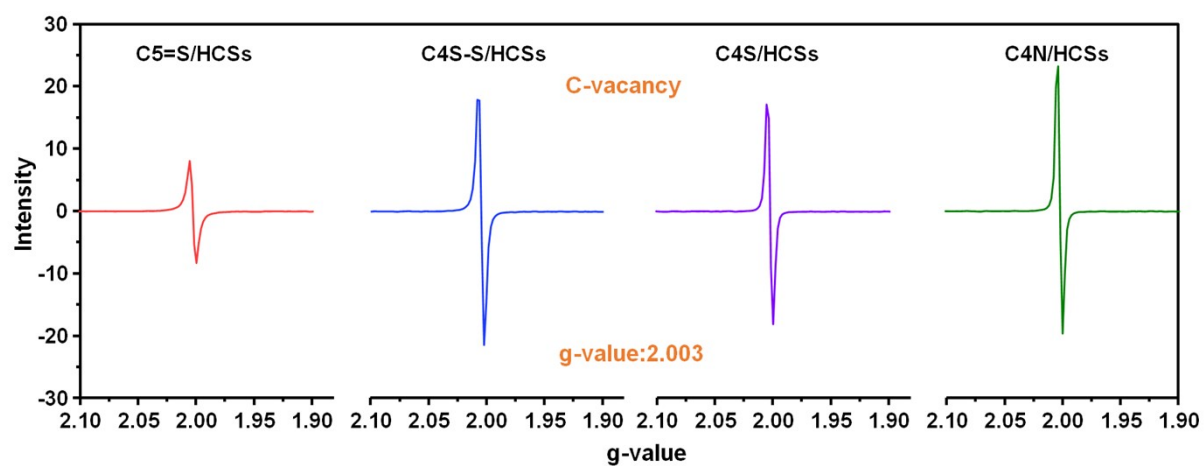
Supplementary Fig. 16. Difference charge density of (a) C=S doped, (b) C-S-S doped and (c) C-S doped graphene skeleton. The yellow area represents the area of electron accumulation, and the blue area represents the area of electron loss.



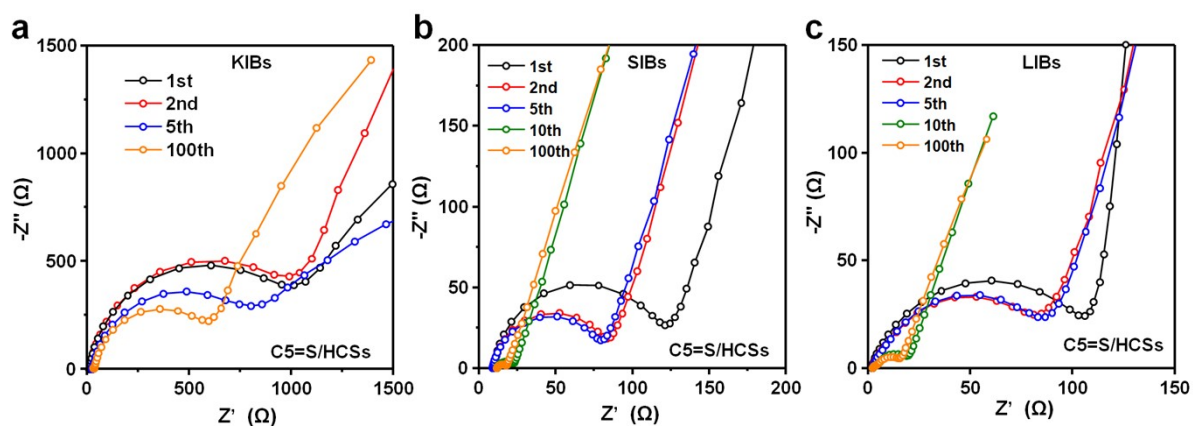
Supplementary Fig. 17. The projected DOS results of (a) C=S doped, (b) C-S doped and (c) C-S-S doped graphene skeleton.



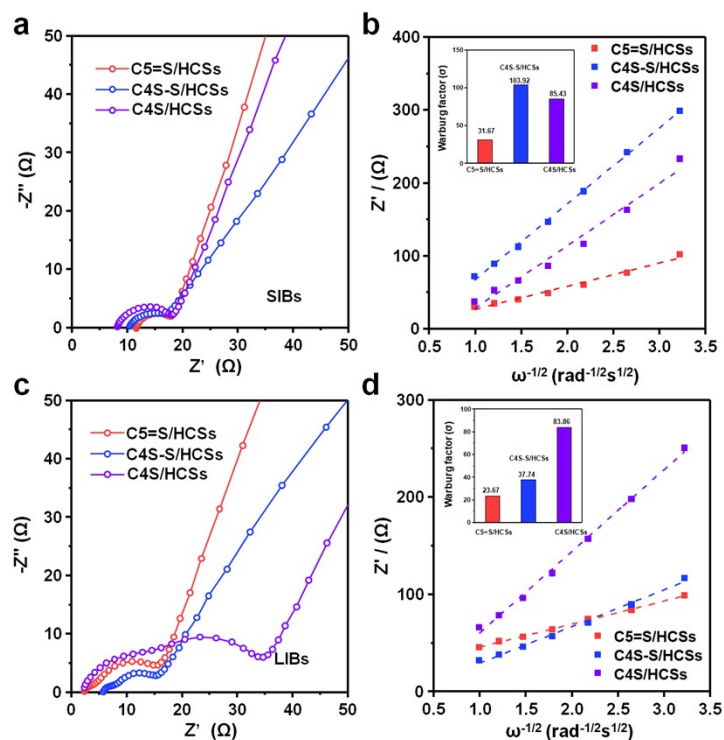
Supplementary Fig. 18. The Electron Localization Function (ELF) images of (a) C=S doped, (b) C-S-S doped and (c) C-S doped graphene skeleton. The slice of 2D charge density diagram of (d) C=S doped, (e) C-S-S doped and (f) C-S doped graphene skeleton.



Supplementary Fig. 19. EPR spectra of C4N/HCSs, C5=S/HCSs, C4S-S/HCSs and C4S/HCSs.



Supplementary Fig. 20. The Nyquist curves of C5=S/HCSs anode from first to 100th cycles in (a) KIBs, (b) SIBs, and (c) LIBs.



Supplementary Fig. 21. The ion and charge transfer kinetics investigated by the electrochemical impedance spectroscopy (EIS). (a) The Nyquist curves and (b) the corresponding linear fits and Warburg factor in the low-frequency region of C5=S/HCSs, C4S-S/HCSs, and C4S/HCSs electrodes after 100 cycles in SIBs. (c) The Nyquist curves and (d) the corresponding linear fits and Warburg factor in the low-frequency region of C5=S/HCSs, C4S-S/HCSs, and C4S/HCSs electrodes after 100 cycles in LIBs.

The linear relationship of alkali metal ion diffusion coefficient with Warburg factor

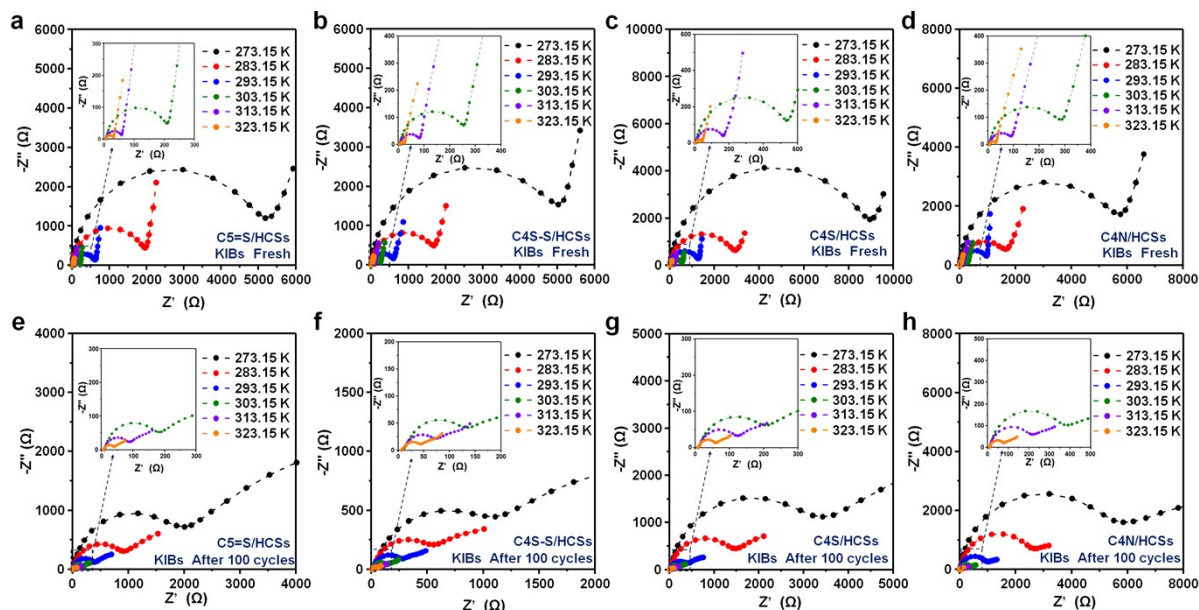
The diffusion coefficient of alkali metal ion can be calculated from the plots in the low frequency region using the following equation:

$$D = \frac{R^2 T^2}{2 A^2 n^4 F^4 C^2 \sigma^2} \text{ (Equation S2)}$$

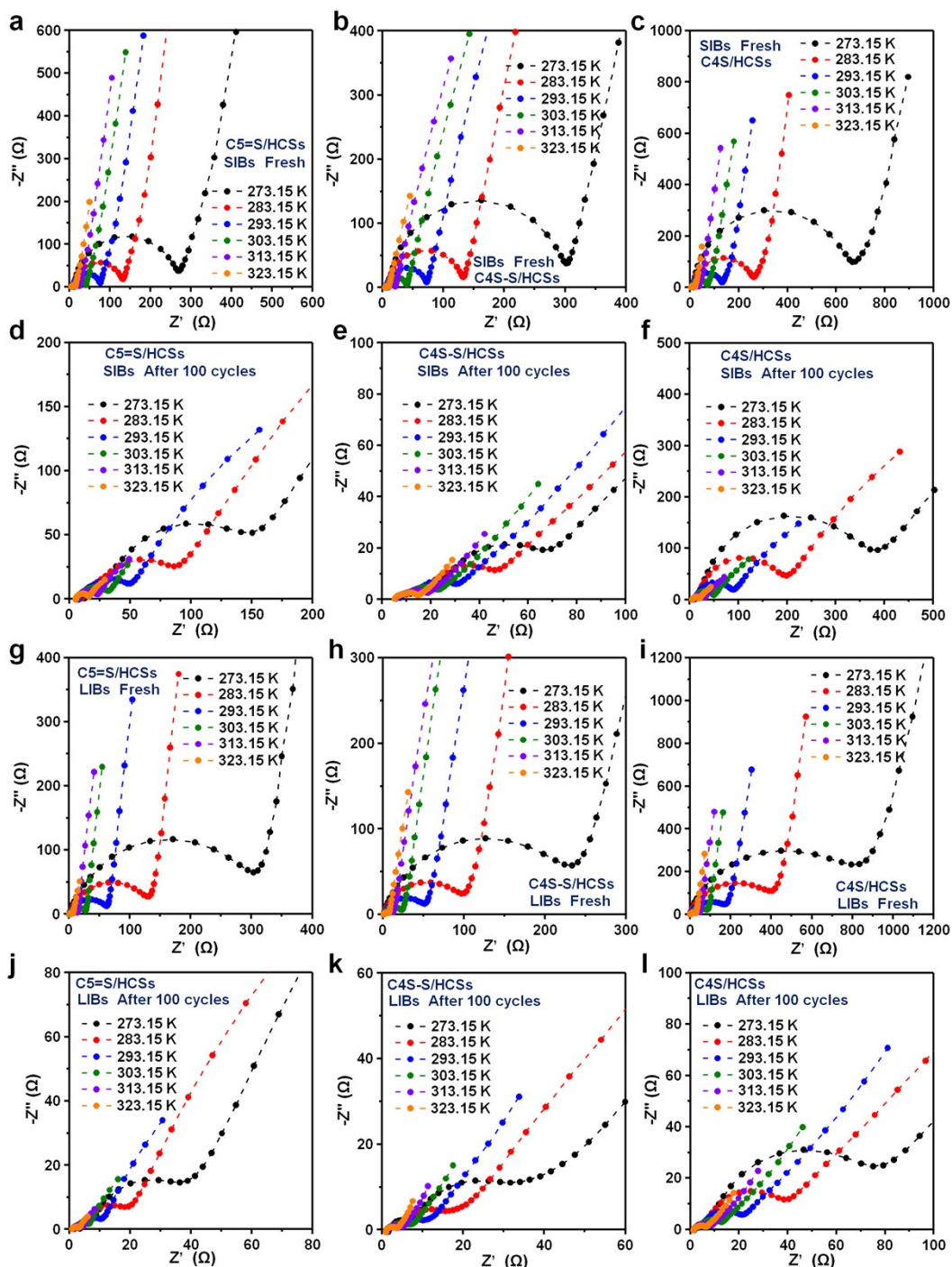
Where R is the gas constant ($8.314 \text{ J mol}^{-1} \text{ K}^{-1}$), T is the absolute temperature (298.15 K), A is the surface area of the working electrode (1.13 cm^2), n is the number of electrons per molecule during oxidation ($9.6486 \times 10^4 \text{ C mol}^{-1}$), F is the Faraday constant ($96,486 \text{ C mol}^{-1}$), C is the concentration of alkali metal ion ($8.97 \times 10^{-2} \text{ mol cm}^{-3}$), and σ is the Warburg factor which obeys the following relationship:

$$Z_{real} = R_e + R_{ct} + \sigma \omega^{-1/2} \text{ (Equation S3)}$$

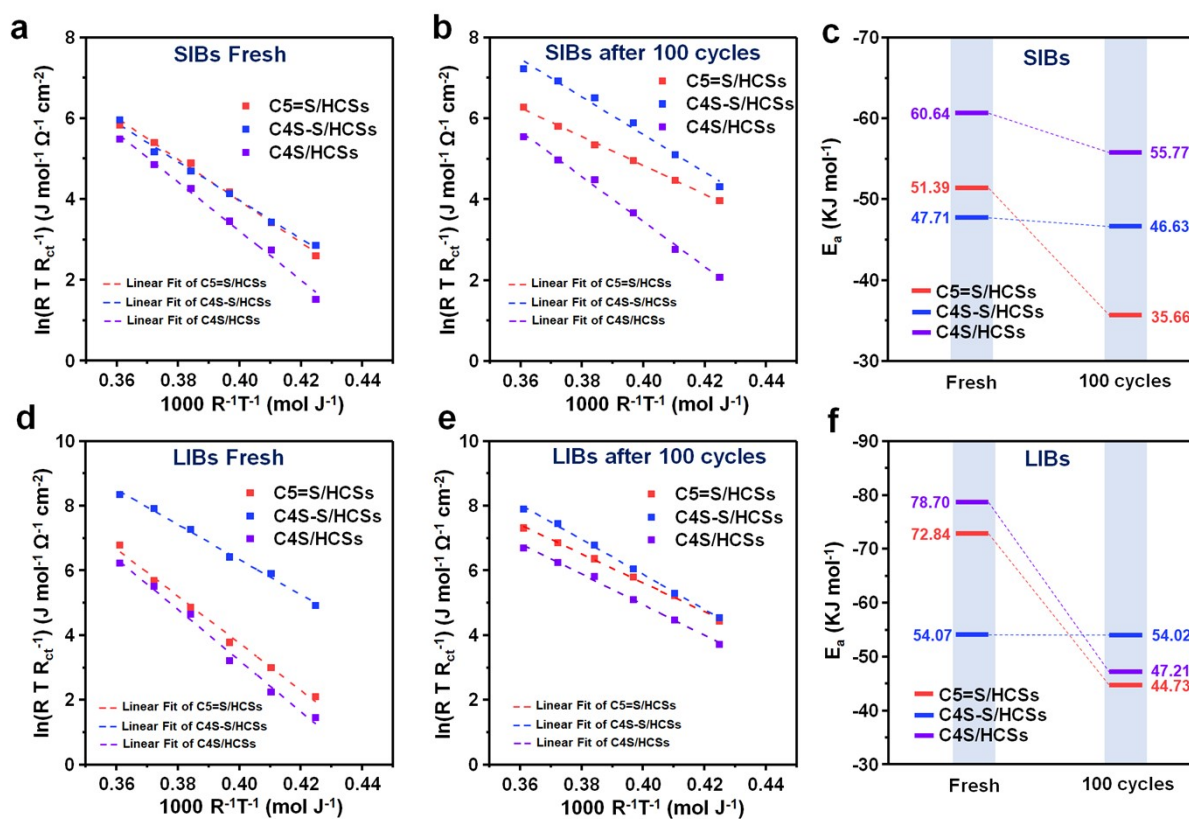
Where R_e is the resistance between the electrolyte and electrode, and R_{ct} is the charge transfer resistance, ω is angle frequency.



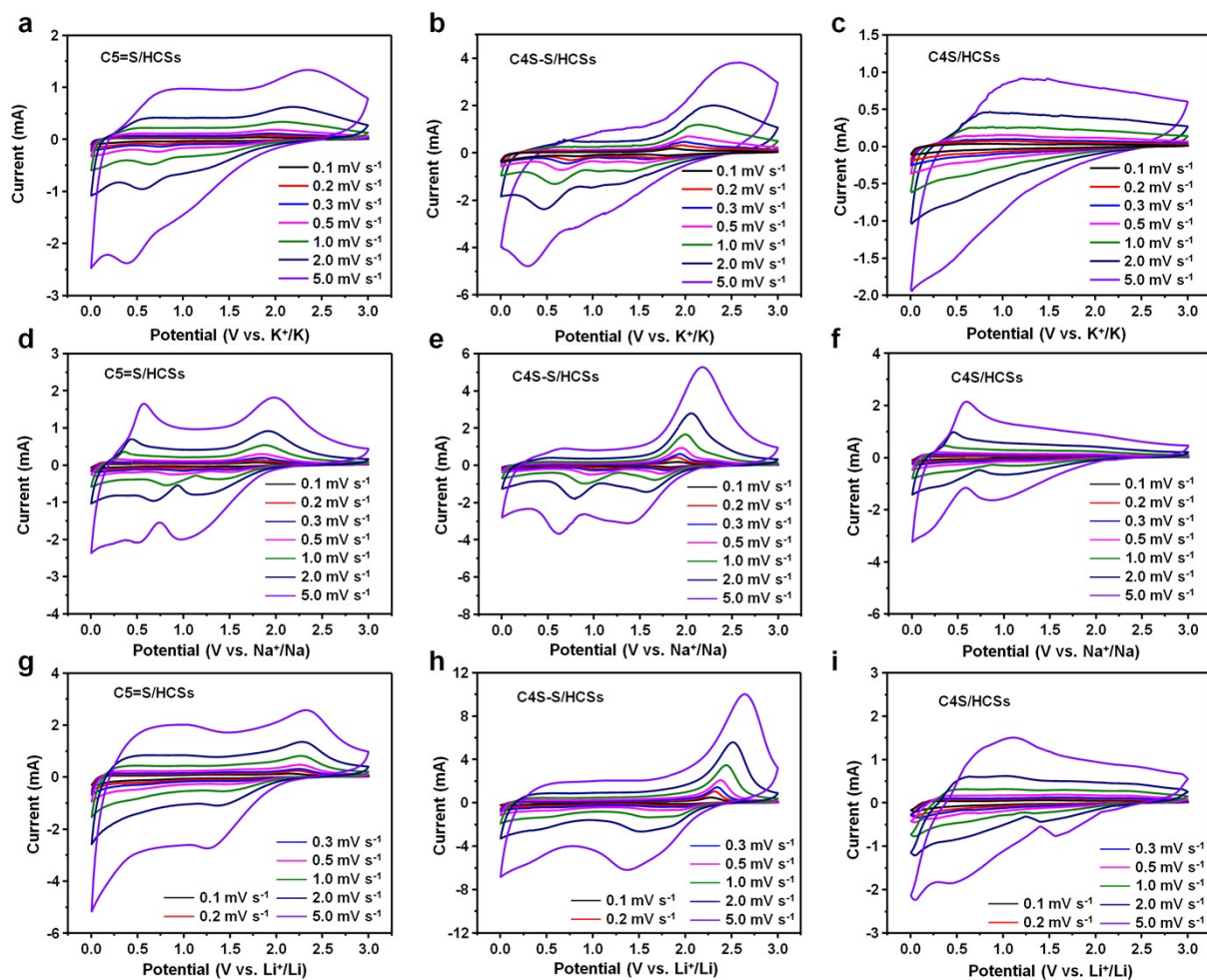
Supplementary Fig. 22. EIS curves of the (a, e) C5=S/HCSs, (b, f) C4S-S/HCSs, (c, g) C4S/HCSs, and (d, h) C4N/HCSs electrodes at fresh and after 100 cycles under various temperatures in KIBs. The raw impedance data and the fitted data is shown as symbols and dotted line.



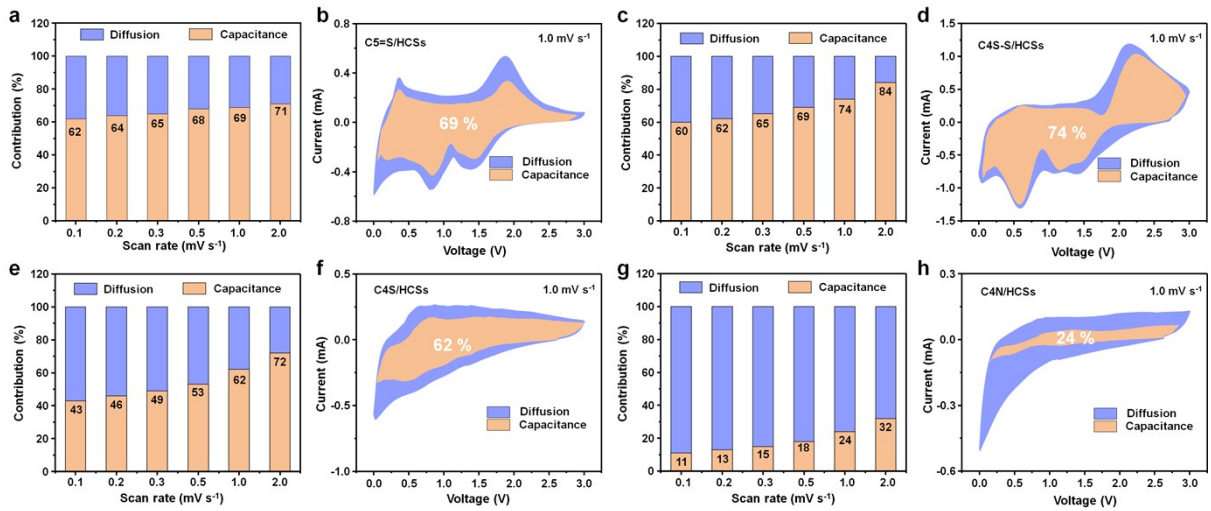
Supplementary Fig. 23. EIS curves of the (a, d) C5=S/HCSs, (b, e) C4S-S/HCSs, and (c, f) C4S/HCSs electrodes at fresh and after 100 cycles under a range of temperatures from 273.15 to 323.15 K in SIBs. The raw impedance data and the fitted data is shown as symbols and dotted line. EIS curves of the (g, j) C5=S/HCSs, (h, k) C4S-S/HCSs, and (i, l) C4S/HCSs electrodes at fresh and after 100 cycles under a range of temperatures from 273.15 to 323.15 K in LIBs. The raw impedance data and the fitted data is shown as symbols and dotted line.



Supplementary Fig. 24. Arrhenius-plots for R_{ct} for C5=S/HCSs, C4S-S/HCSs, and C4S/HCSs electrodes at (a) fresh cycle and (b) after 100 cycles in SIBs. (c) Activation energy for C5=S/HCSs, C4S-S/HCSs, C4S/HCSs, and C4N/HCSs electrodes at fresh and after 100 cycles in SIBs. (d-f) The corresponding results in LIBs



Supplementary Fig. 25. The CV curves of C5=S/HCSs (a, d, and g), C4S-S/HCSs (b, e, and h) and C4S/HCSs (c, f and i) electrodes in KIBs, SIBs and LIBs at a range of scan rates from 0.1 to 5.0 mV s⁻¹.



Supplementary Fig. 26. The capacitance contribution ratios analysis. The data is the pseudocapacitive and diffusive controlled contribution ratios of (a) C5=S/HCSs, (c) C4S-S/HCSs, (e) C4S/HCSs and (g) C4N/HCSs at the scan rate of 0.1, 0.2, 0.3, 0.5, 1.0, 2.0 mV s⁻¹. Pseudocapacitive and diffusive contribution at 1.0 mV s⁻¹ of (b) C5=S/HCSs, (d) C4S-S/HCSs, (f) C4S/HCSs and (h) C4N/HCSs under the potential of 0.005-3.0 V.

Calculation of pseudocapacitive and diffusive controlled contribution

$$i = av^b \text{ (Equation S5)}$$

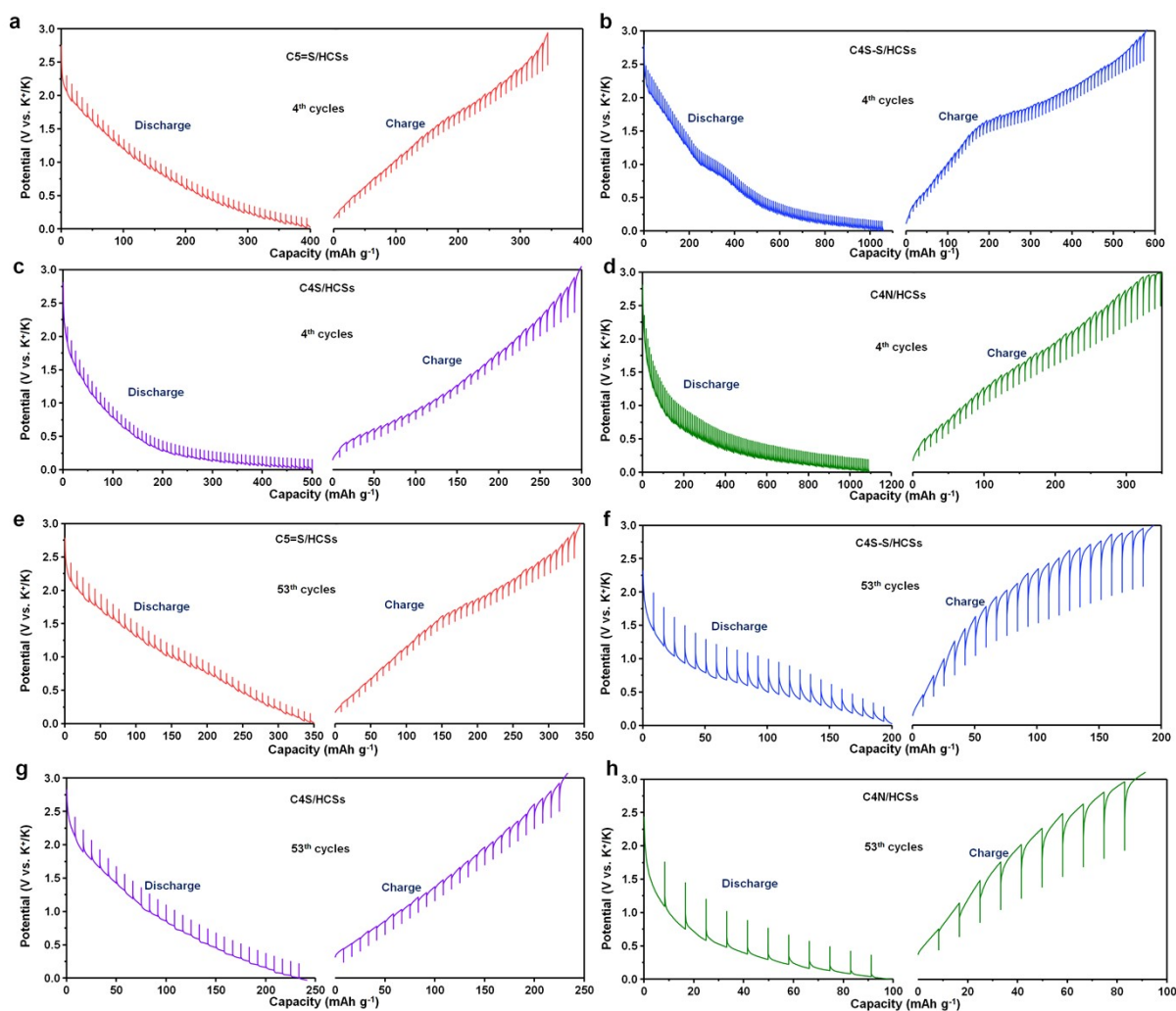
Which is equal to:

$$\log(i) = b \log(v) + \log(a) \text{ (Equation S6)}$$

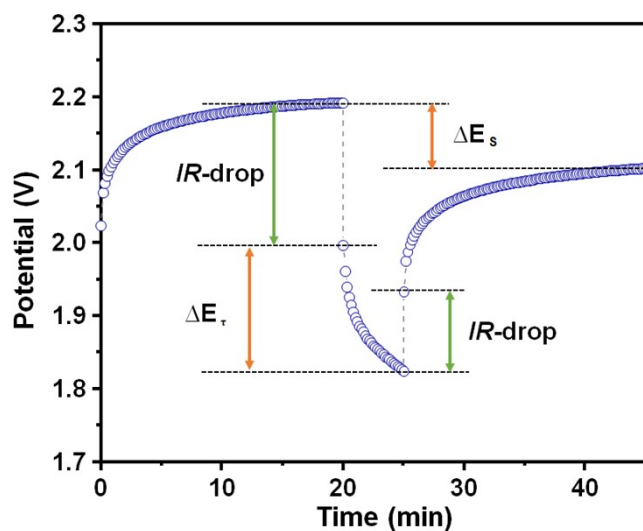
Where a and b are changeable indicators. It represents the process of capacitive or diffusive process when the b value approaches 1 or 0.5, respectively. The quantitative calculation of surface capacitance and sodium ion semi-infinite diffusion is based on the following equation :

$$i = k_1 v + k_2 v^{1/2} \text{ (Equation S7)}$$

Where $k_1 v$ and $k_2 v^{1/2}$ are separately attributed to pseudocapacitive and diffusive controlled contribution.



Supplementary Fig. 27. GITT patterns of C5=S/HCSs, C4S-S/HCSs, C4S/HCSs, and C4N/HCSs electrodes in (a-d) the 4th cycle and (e-h) 53th cycle of KIBs, respectively.



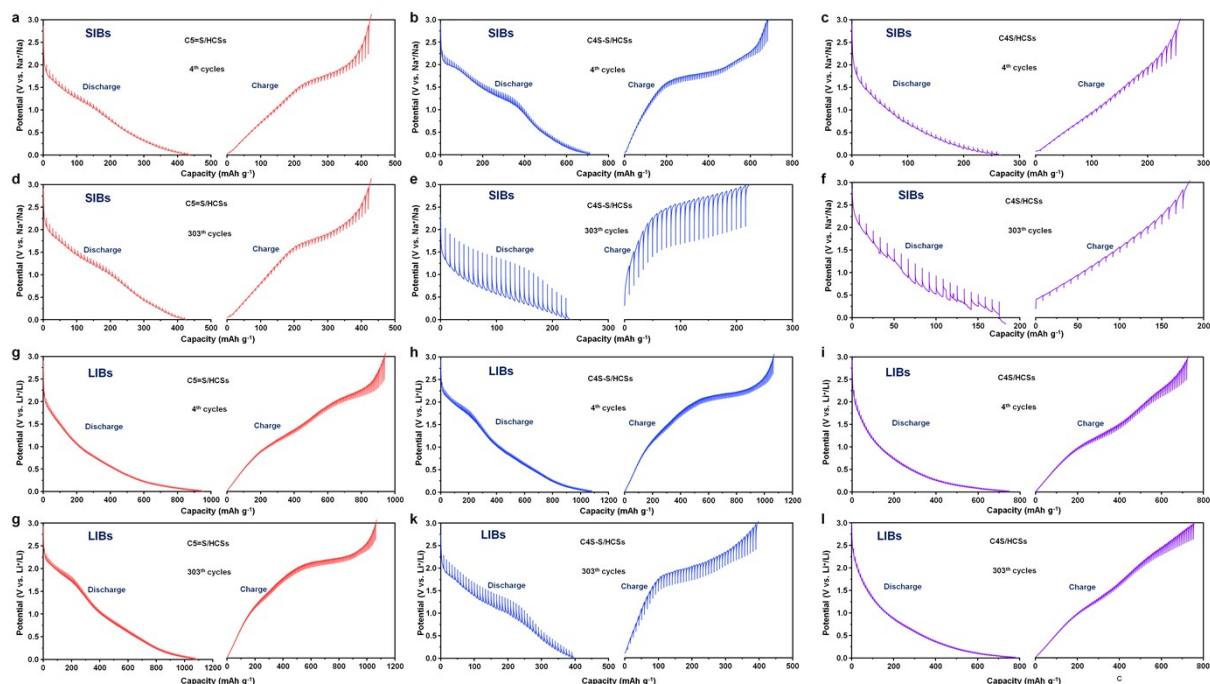
Supplementary Fig. 28. The value of D_k can be calculated according to the simplified Fick's second law with the following equation:

$$D = \frac{4}{\pi\tau} \left\{ \frac{m_B V_m}{M_B A} \right\}^2 \left(\frac{\Delta E_s}{\Delta E_\tau} \right)^2 \quad (\text{Equation S8})$$

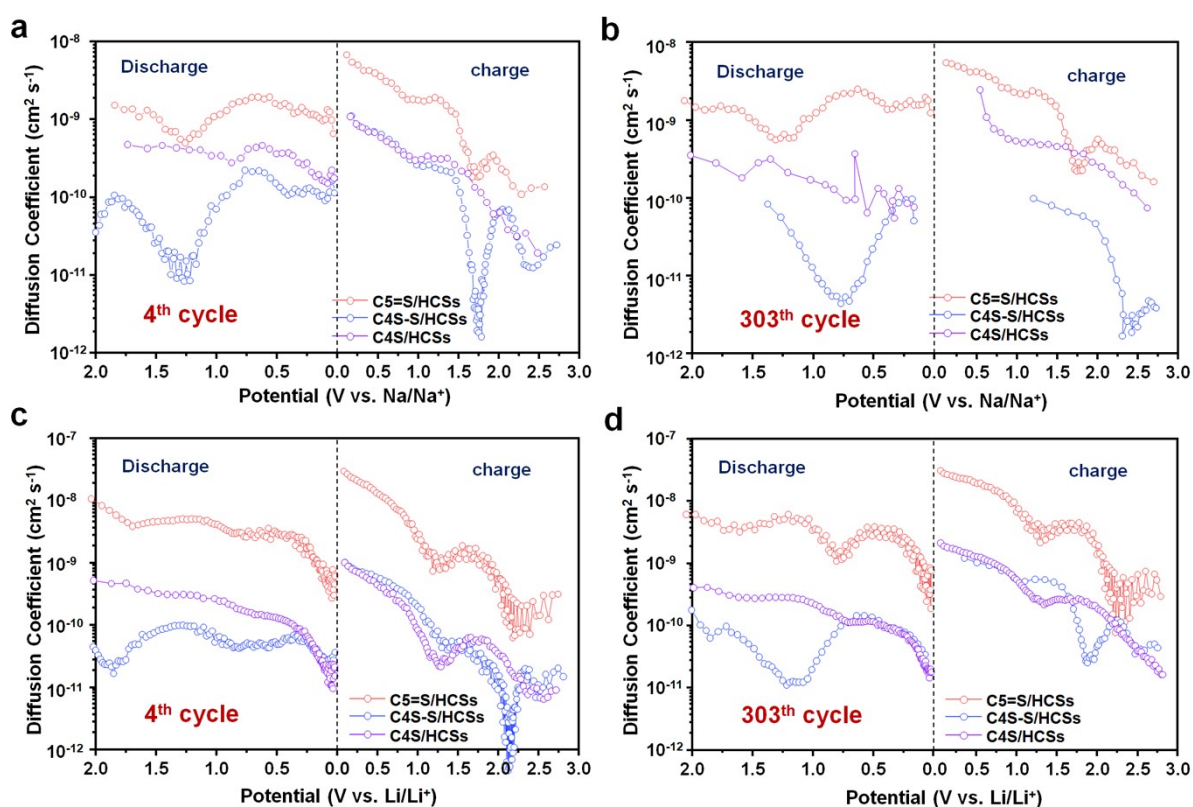
where τ is the duration of the current pulse, m_B is the electrode active mass, M_B and V_M denotes the molar mass and molar volume of electrode material, A is the geometric area of electrode. ΔE_s is the quasi-thermodynamic equilibrium potential difference between before and after the current pulse regardless of the IR-drop. ΔE_τ represents the change of voltage during the current pulse. The relative value of M_B/V_M can be obtained from the density of materials, which is calculated according to the following equation:

$$\rho = \frac{1}{V_{total} + \frac{1}{\rho_{carbon}}} \quad (\text{Equation S9})$$

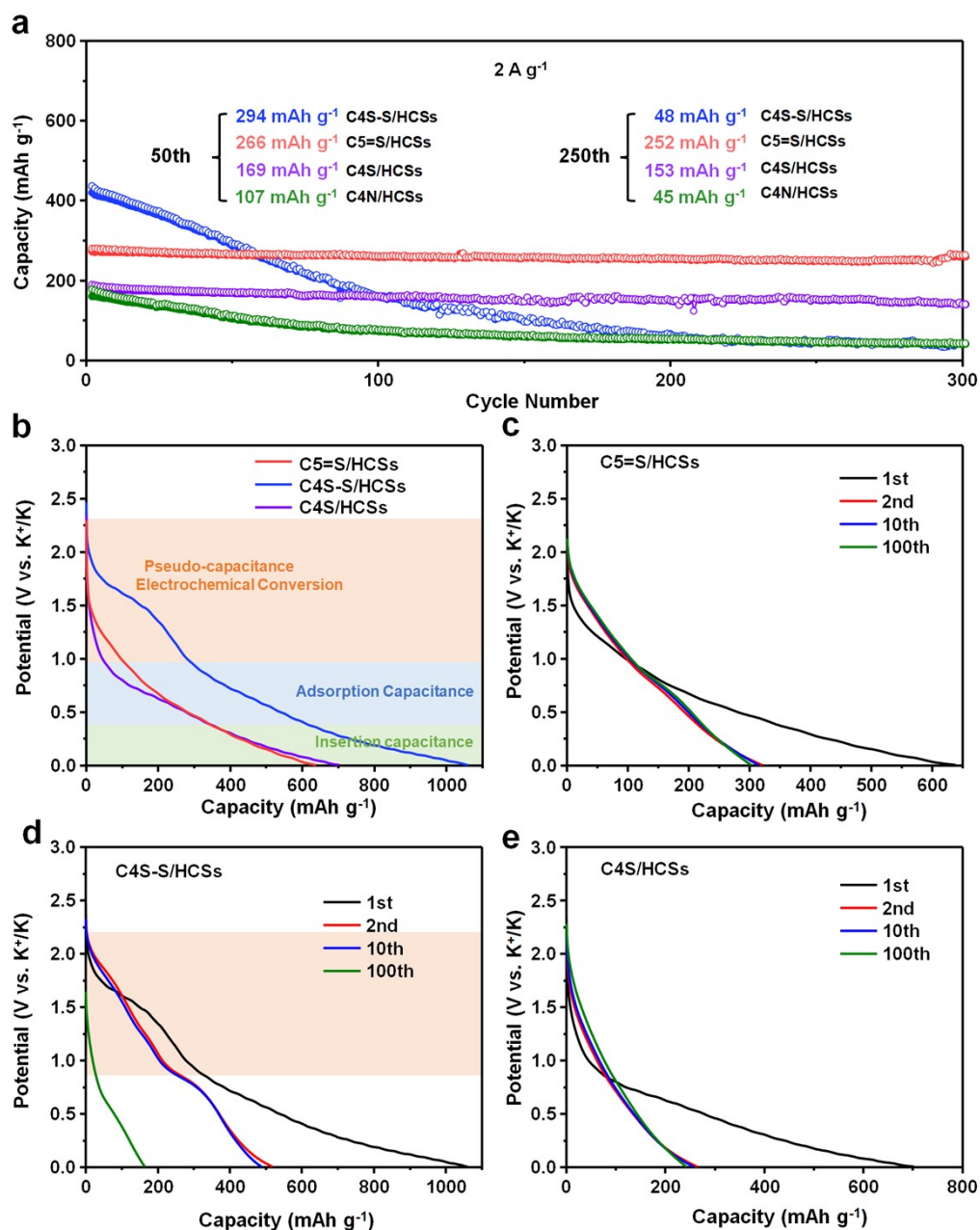
where ρ (g cm^{-3}) is the density of materials, V_{total} ($\text{cm}^3 \text{ g}^{-1}$) is the total pore volume determined from the N_2 isotherm in Table S9, and ρ_{carbon} is the true density of carbon (2 g cm^{-3}).



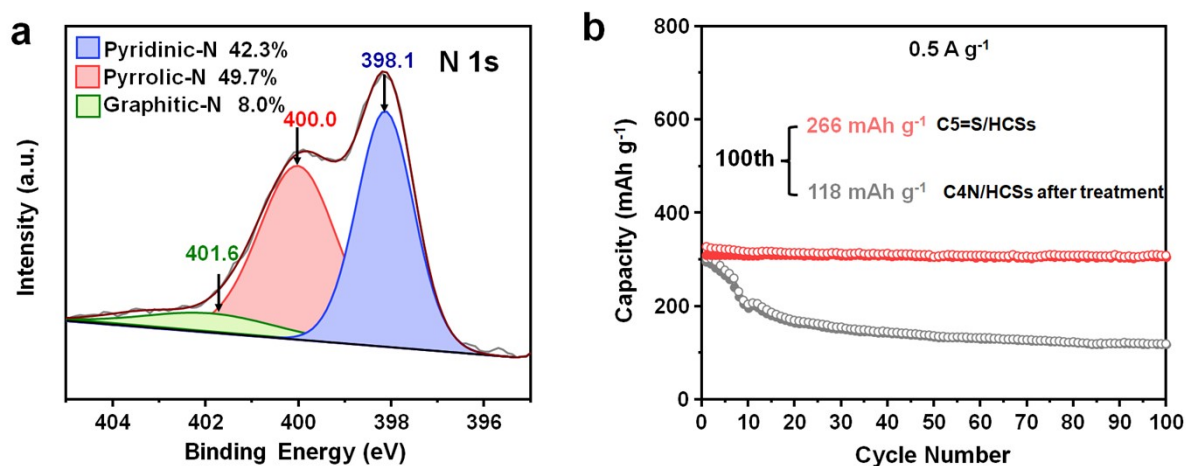
Supplementary Fig. 29. GITT patterns of (a) C5=S/HCSs, (b) C4S-S/HCSs and (c) C4S/HCSs in the 4th cycle of SIBs, and (d) C5=S/HCSs, (e) C4S-S/HCSs and (f) C4S/HCSs in the 303th cycle of SIBs. And the GITT patterns of (g) C5=S/HCSs, (h) C4S-S/HCSs and (i) C4S/HCSs in the 4th cycle of LIBs, and (j) C5=S/HCSs, (k) C4S-S/HCSs and (l) C4S/HCSs in the 303th cycle of LIBs.



Supplementary Fig. 30. The diffusion Coefficient of C5=S/HCSs, C4S-S/HCSs and C4S/HCSs in the (a) 4th cycle and (b) 303th cycle of SIBs, and in the (c) 4th cycle and (d) 303th cycle of LIBs.



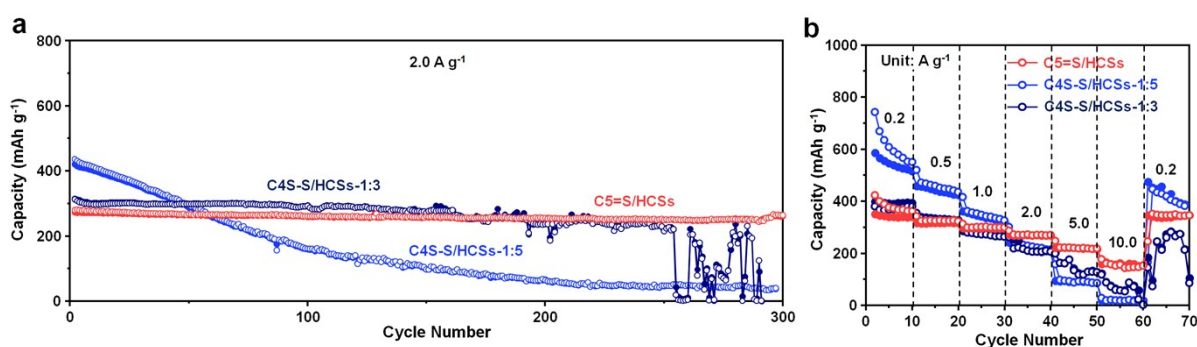
Supplementary Fig. 31. (a) The comparison of cycle performance of C5=S/HCSs, C4S-S/HCSs, and C4S/HCSs at a current density of 2.0 A g⁻¹. (b) The galvanostatic discharge profiles of C5=S/HCSs, C4S-S/HCSs, C4S/HCSs anodes at a current density of 0.2 A g⁻¹. (c-e) The galvanostatic discharge profiles of (c) C5=S/HCSs, (d) C4S-S/HCSs, and (e) C4S/HCSs anodes during the extended cycles.



Supplementary Fig. 32. The XPS N 1s high resolution-spectra of (c) C5=S/HCSs and (a) the HCSs with the similar N contents without S. (b) The comparison of cycle performance of these two samples at a current density of 0.5 A g⁻¹ in KIBs.

Note: For distinguishing the excellent electrochemical performance is the C=S species rather than the N-containing species. This work secondary heat treatment the C4N/HCSs precursor without CS₂ under the similar temperature for 6 hours, and obtained the carbon skeleton with similar N content but without S.

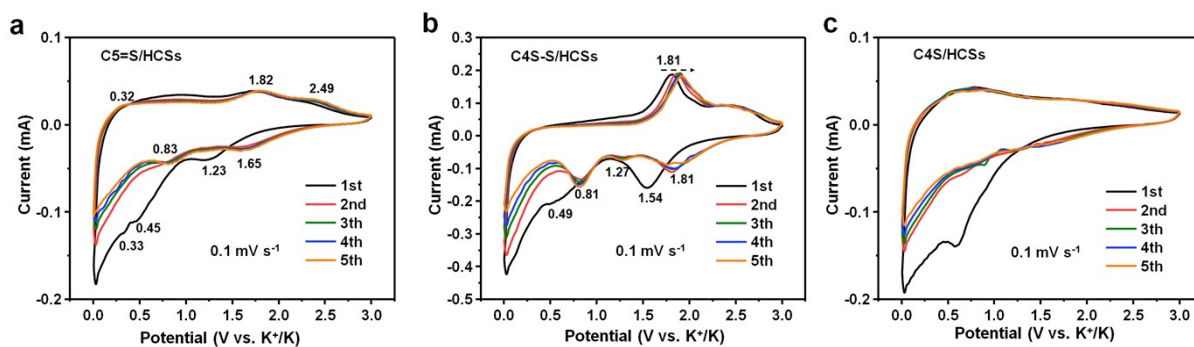
Indeed, N doped carbon materials have been widely applied into alkali metal ion batteries with high discharge capacity and long-term cycling performance. The N doping contributes to the conductivity and surface wettability, while the S doping is bridged to build stable active sites, which can be electrochemically converted into mercaptan anions via faraday reaction and further enhancing reversible capacities.¹⁻³ In this study, the delocalized C=S could optimize the space π electron conjugation and the formation of spatial sp^2 -hybridization between carbon layers, thereby providing superior electronic and atomic structural properties. Thus, the C=S doped carbon materials delivered superior electrochemical performance, accompanying with an order of magnitude greater electronic conductivity and ionic diffusion coefficient. This finding offers valuable insights into the design of 3D spatial charge transfer in carbon skeleton for achieving fast reversible ion storage kinetics.



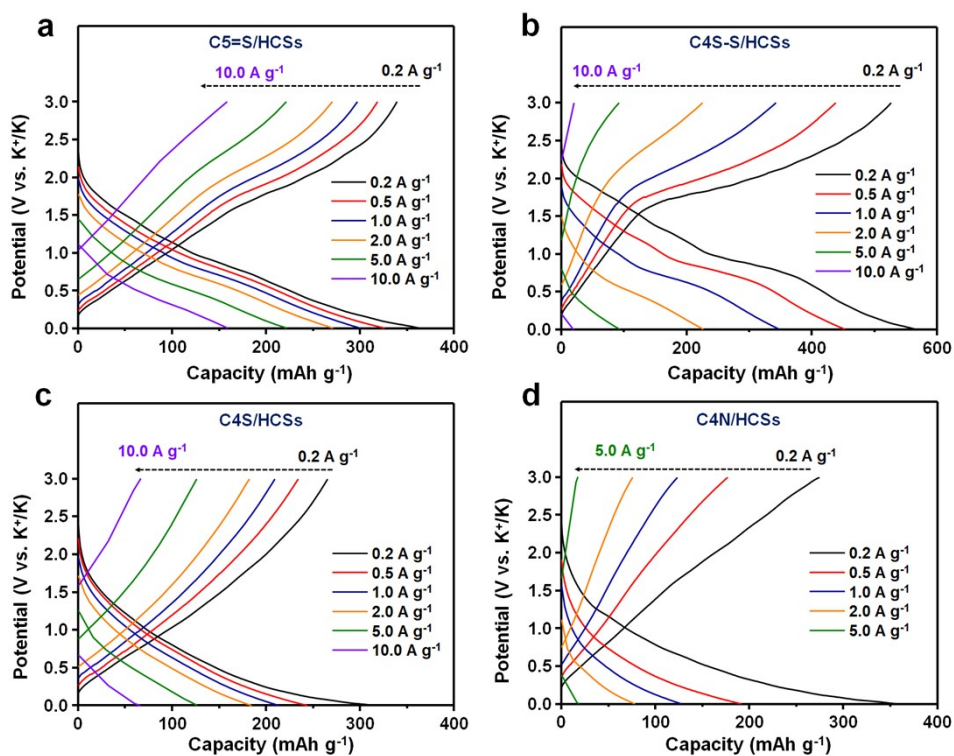
Supplementary Fig. 33. (a) The cycling performance of C5=S/HCSs, C4S-S/HCSs-1:3, and C4S-S/HCSs-1:5 at a current density of 2.0 A g⁻¹, and the multi-rate performance at 0.2 to 10.0 A g⁻¹ in KIBs.

Table. The normalization EA results of C5=S/HCSs, C4S-S/HCSs-1:3 and C4S-S/HCSs-1:5.

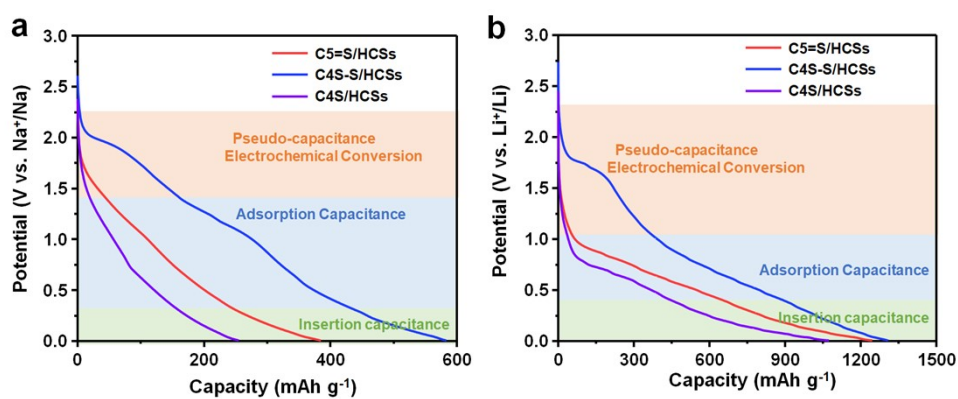
Atom Percent	N		S	
	wt. %	at. %	wt. %	at. %
C5=S/HCSs	4.66	4.72	23.42	10.36
C4S-S/HCSs-1:3	5.10	6.72	25.24	12.35
C4S-S/HCSs-1:5	4.80	6.00	33.12	18.10



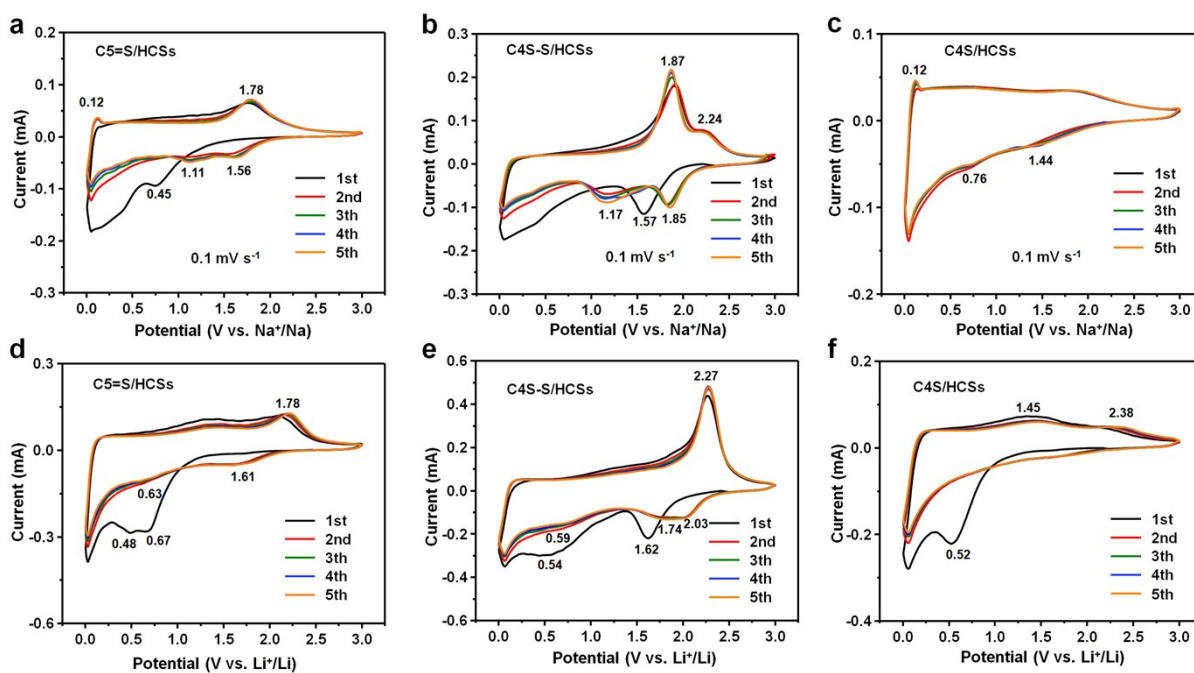
Supplementary Fig. 34. CV curves of initial 5 cycles at 0.1 mV s⁻¹ of (a) C5=S/HCSs, (b) C4S-S/HCSs and, (c) C4S/HCSs electrodes in KIBs.



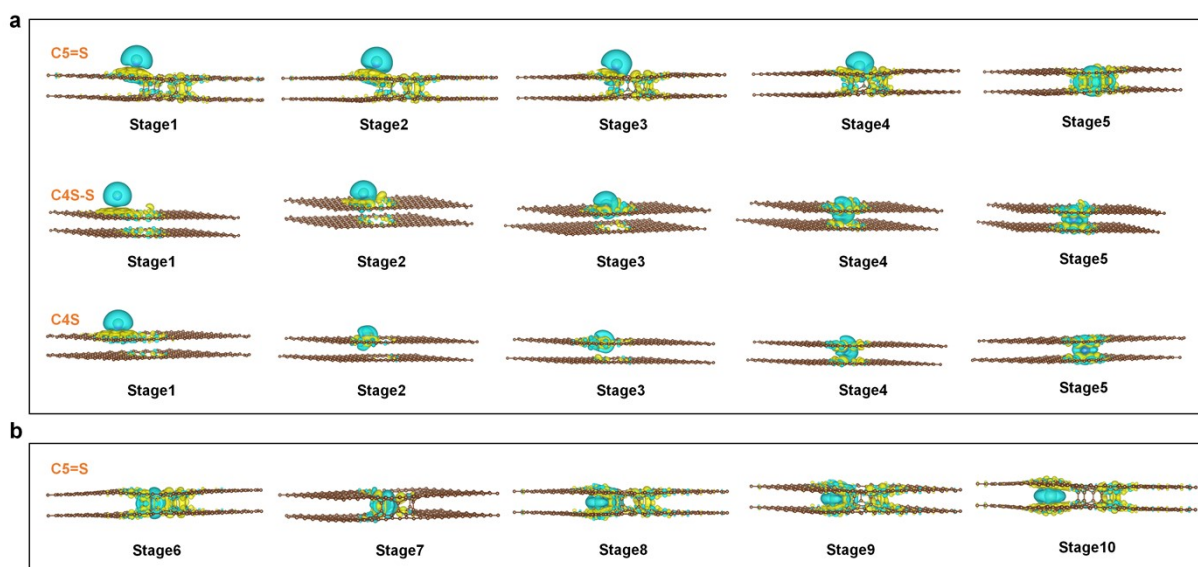
Supplementary Fig. 35. The galvanostatic discharge/charge profiles of (a) C5=S/HCSs, (b) C4S-S/HCSs, (c) C4S/HCSs, and (d) C4N/HCSs electrodes at 0.2-10.0 A g⁻¹ in KIBs.



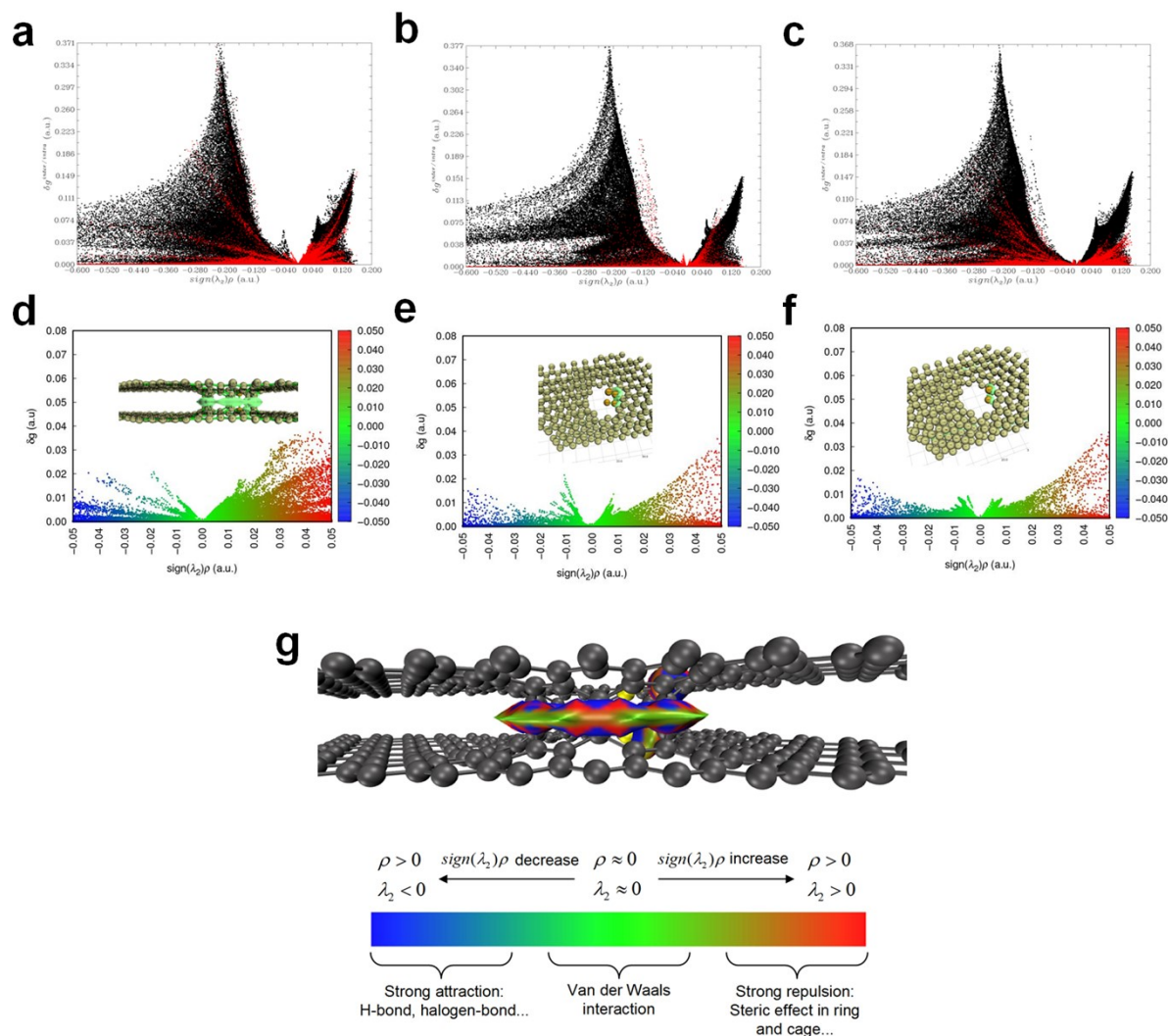
Supplementary Fig. 36. The galvanostatic discharge profiles of C5=S/HCSs, C4S-S/HCSs, C4S/HCSs anodes at a current density of 0.2 A g⁻¹ in (a) SIBs and (b) LIBs.



Supplementary Fig. 37. CV curves of initial 5 cycles at 0.1 mV s^{-1} of (a, d) C5=S/HCSs, (b, e) C4S-S/HCSs and, (c, f) C4S/HCSs electrodes.



Supplementary Fig. 38. (a) The corresponding electron density differences of C=S doped, C-S-S doped, and C-S doped bilayer graphene with K, while K-ion diffusion paths from top layer to the 3D defect of three carbon skeletons. (b) The corresponding electron density differences of C=S doped bilayer graphene with K, while K-ion diffusion paths from 3D defect to interlayer of three carbon skeletons.

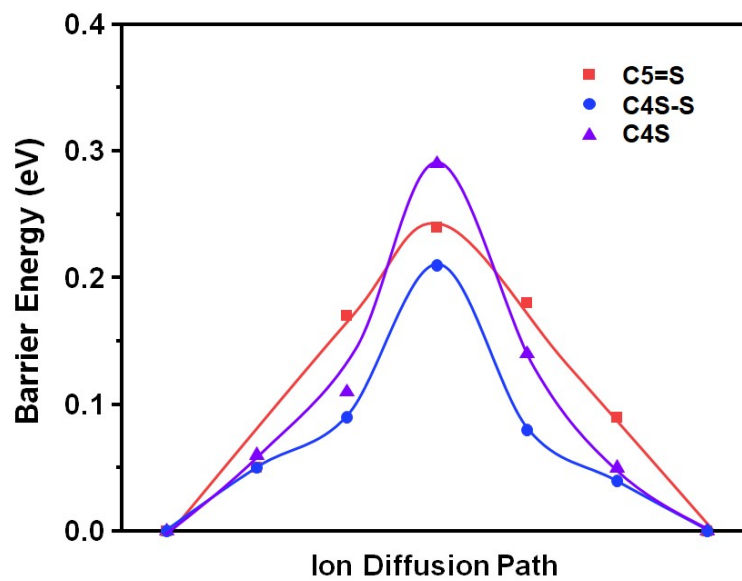


Supplementary Fig. 39. (a-c) The weak interactions between carbon layers of (a) C5=S, (b) C4S-S, and (c) C4S by using the independent gradient model (IGM) of Multiwfn software. The blue, green and yellow scales are used to represent the steric effects of strong attraction, van der Waals and mutual repulsion in (d) C5=S, (e) C4S-S, and (f) C4S, respectively. (g) The colorful isosurface mapping of $\text{sign}(\lambda_2)\rho$ for C5=S skeleton by Visual Molecular Dynamics (VMD).

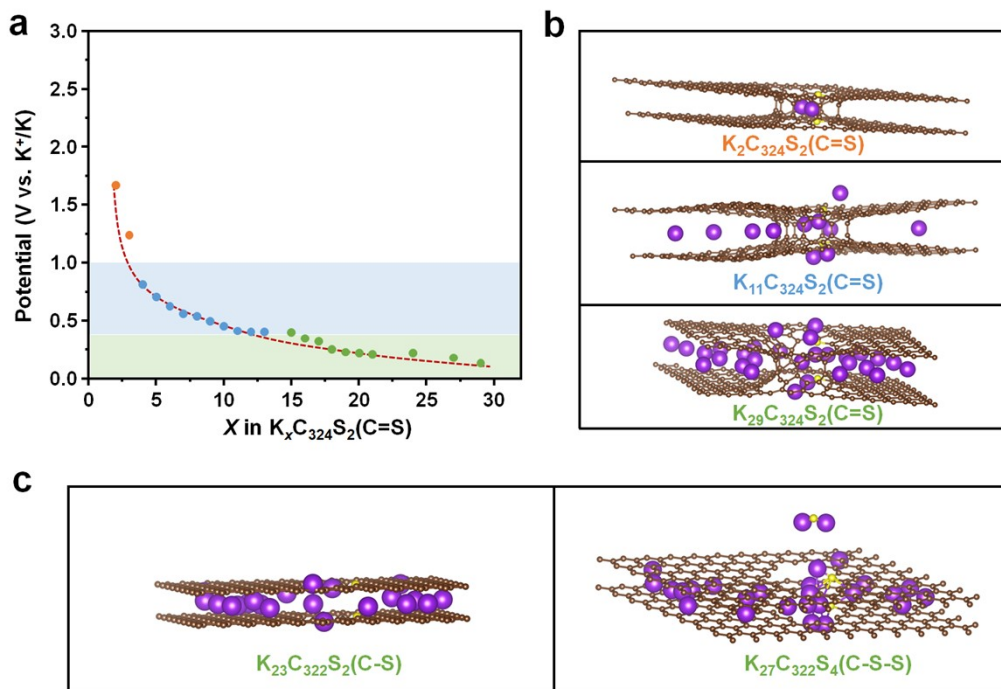
To consider the spatial steric hindrance caused by the proximity of certain atoms or groups in carbon skeleton, Multiwfn software was used to investigate the weak interactions between carbon layers by using the independent gradient model (IGM).⁴ The plot scatter of δg vs. $\text{sign}(\lambda_2)\rho$ was displayed in **Fig. S39 a-c**. The blue, green and yellow scales are used to represent the steric effects of strong attraction, van der Waals and mutual repulsion in the carbon skeleton, respectively in **Fig. S39 d-f**.⁵ While $\text{sign}(\lambda_2)\rho > 0$, there are many plots in three structure which demonstrated the existence of steric hindrance effect in three carbon skeletons.

Moreover, colorful isosurface mapping of $\text{sign}(\lambda_2)\rho$ for C5=S skeleton by Visual Molecular Dynamics (VMD) was shown in **Fig. S39g**. The color of the isosurface of the region forming

the upper and lower interconnection structure is obvious blue, so it should be considered that a special spatial interconnection structure is formed in the carbon layer of C5=S. Secondly, there is a large area of green flat sheet, reflecting the corresponding weak interaction region of the electron density is very small, the value is close to 0. Thus, the effect strength is too weak, and could be ascribed to be interpreted as dispersion. The red area shows that the C5=S structure exist a little steric hindrance effect.



Supplementary Fig. 40. The corresponding energy barriers along these paths of C=S doped, C-S-S doped, and C-S doped bilayer graphene with K, while K-ion diffusion paths from top layer to the 3D defect of three carbon skeletons.



Supplementary Fig. 41. (a) Computed discharge potential curves consisting of discontinuous potential points, with a certain number of states of potassium atoms in C=S doped carbon skeleton, and (b) corresponding structures with different numbers of potassium atoms. (c) The final state after potassization of C-S and C-S-S doped carbon skeleton.

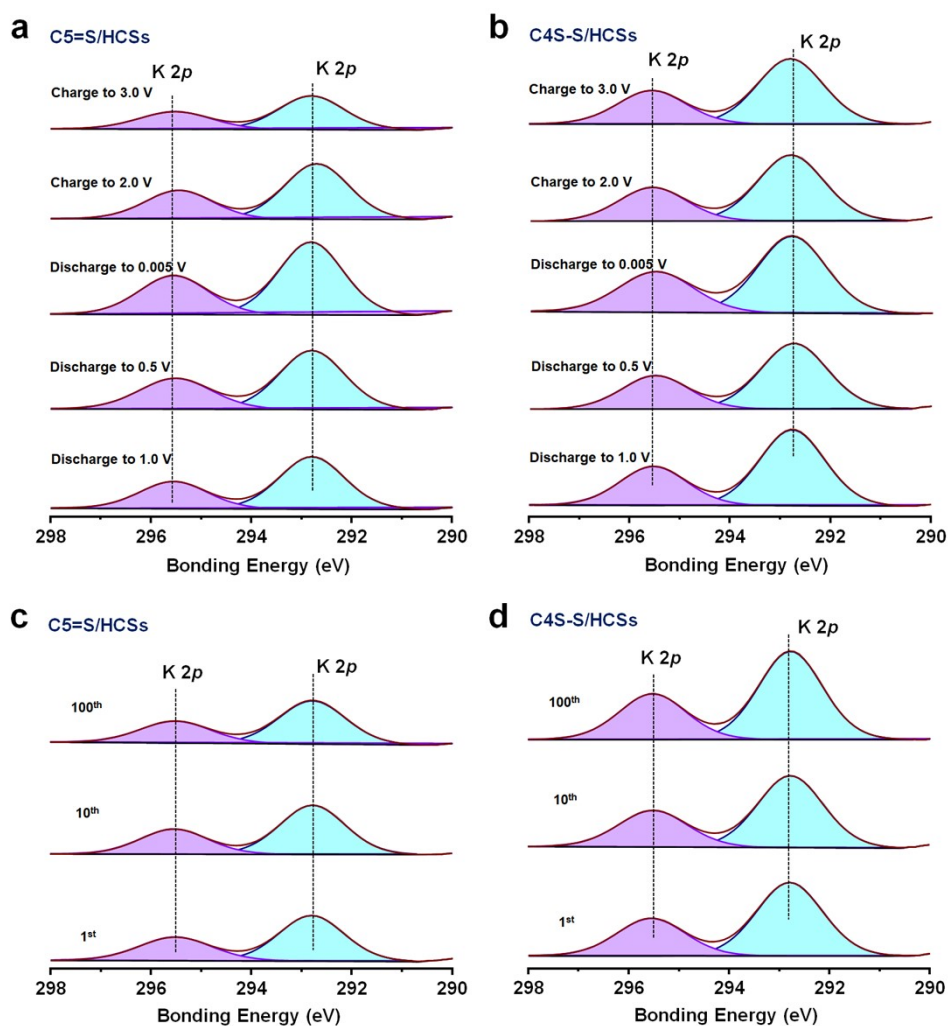
Note: The experimental data relevant to this study is the voltage filling relationship for disordered structures as a function of cell voltage and atomic filling. In general, the voltage U is calculated by the formula⁶

$$U = - [G(M_x C_y) - xG(M) - yG(C)] / nF$$

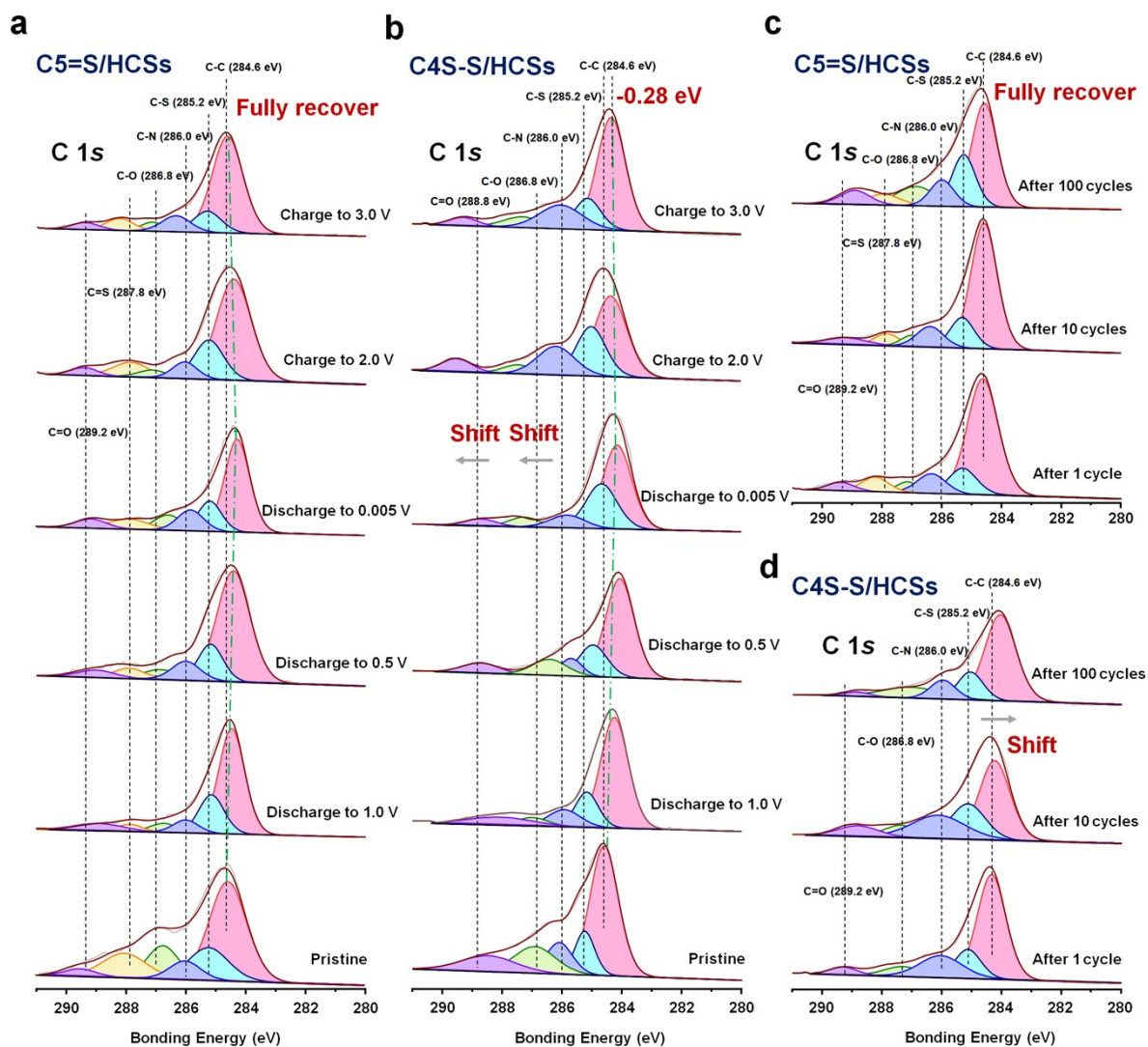
Where G is the Gibbs energy for a given component, n denotes the number of electrons transferred, and F is the Faraday constant. In the calculations, this method is based on the energy at zero Kelvin and therefore does not take into account the temperature factor.⁷ Thus, the above expression is usually approximated as:

$$U = - [E(M_x C_y) - xE(M) - yE(C)] / x$$

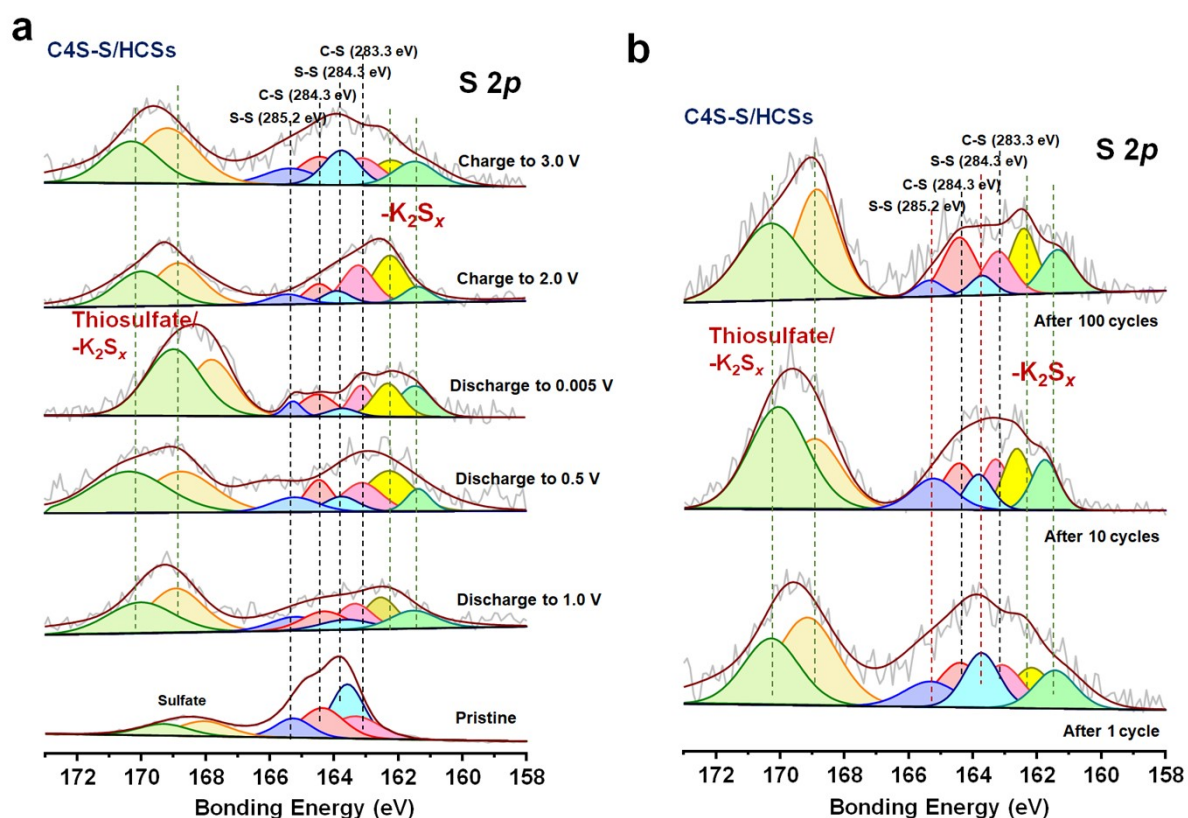
Where E represents the total energy of the system in the same case.



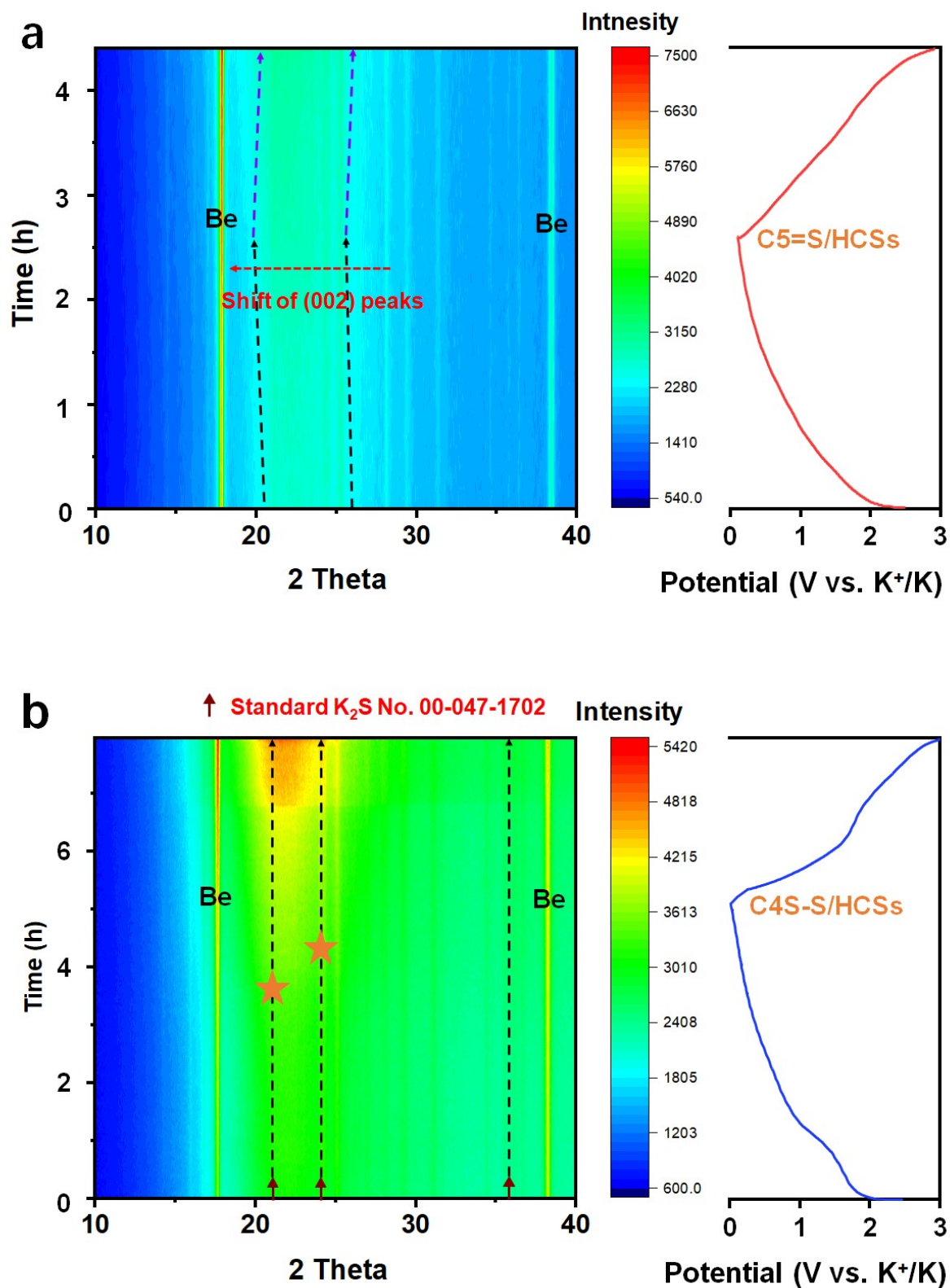
Supplementary Fig. 42. K 2 p high-resolution XPS spectra of (a) C5=S/HCSs and (b) C4S-S/HCSs electrodes during the initial discharging/charging. K 2 p High-resolution XPS spectra of (c) C5=S/HCSs and (d) C4S-S/HCSs electrodes after 1, 10, 100 cycles.



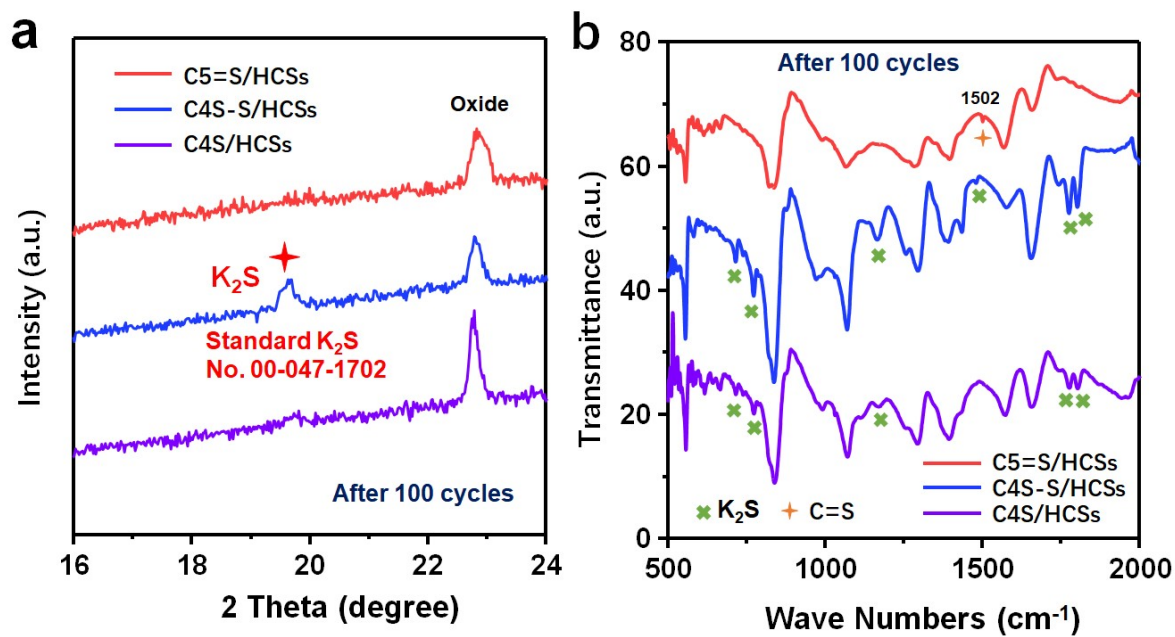
Supplementary Fig. 43. (a) *Ex-situ* high-resolution C 1s XPS of (a) C5=S/HCSs and (b) C4S-S/HCSs electrodes during the initial discharging and charging. High-resolution C 1s XPS spectra of (c) C5=S/HCSs and (d) C4S-S/HCSs electrodes after 1, 10, 100 cycles.



Supplementary Fig. 44. (a) The reversibility of High-resolution S 2p spectra at different potential state during the initial discharging and charging and (b) the spectra of C4S-S/HCSs electrodes after 1, 10, 100 cycles.



Supplementary Fig. 45. *In-situ* measurements of the cycled electrodes. (a) The *in-situ* XRD characterization of the potassium storage mechanism of (a) C5=S/HCSs and (b) C4S-S anode for the initial cycle.



Supplementary Fig. 46. (a) XRD patterns and (b) FT-IR spectra of C5=S/HCSs, C4S-S/HCSs, and C4S/HCSs electrodes after 1, 10, 100 cycles.

Supplementary Tables

Table S1. The raw results of elemental contents for different carbon and sulfur bonds doped carbonaceous materials based on EA results.

Atom Percent (wt.%)	N	C	H	S	O
C4N/HCSs	7.12	79.45	3.44		9.99
C4S/HCSs	7.58	81.31	1.89	5.45	3.77
C5=S/HCSs	4.48	69.22	1.4	22.54	2.36
C4S-S/HCSs	4.45	57.62	1.11	30.74	6.08

Table S2. The normalization results of N, C, S contents for different carbon and sulfur bonds doped carbonaceous materials based on EA results.

Atom Percent	N		C		S	
	<i>wt. %</i>	<i>at. %</i>	<i>wt. %</i>	<i>at. %</i>	<i>wt. %</i>	<i>at. %</i>
C4N/HCSs	8.22	7.13	91.78	92.87	/	/
C4S/HCSs	8.02	7.21	86.20	90.51	5.78	2.28
C5=S/HCSs	4.66	4.72	71.92	71.92	23.42	10.36
C4S-S/HCSs	4.80	6.00	52.08	75.90	33.12	18.10

Table S3. The pyridinic-N, pyrrolic-N, and graphite-N contents for different carbon and sulfur bonds doped carbonaceous materials based on EA results.

Atom Percent	Pyridinic-N		Pyrrolic-N		Graphite-N	
	<i>wt.%</i>	<i>at.%</i>	<i>wt.%</i>	<i>at.%</i>	<i>wt.%</i>	<i>at.%</i>
C4N/HCSs	1.47	1.28	6.26	5.43	0.49	0.42
C4S/HCSs	2.70	2.42	4.56	4.10	0.76	0.69
C5=S/HCSs	1.84	1.86	2.34	2.37	0.48	0.49
C4S-S/HCSs	1.73	2.15	2.53	3.17	0.54	0.68

Table S4. The raw results of elemental contents for different carbon and sulfur bonds doped carbonaceous materials based on XPS results.

Atom Percent (wt.%)	N	C	S	O
C4N/HCSs	7.36	81.8	/	10.84
C4S/HCSs	7.93	84.97	2.13	4.97
C5=S/HCSs	6.14	81.2	7.95	4.82
C4S-S/HCSs	6.25	72.21	15.02	6.52

Table S5. The normalization results of N, C, S contents for different carbon and sulfur bonds doped carbonaceous materials based on XPS results.

Atom Percent	N		C		S	
	<i>wt. %</i>	<i>at. %</i>	<i>wt. %</i>	<i>at. %</i>	<i>wt. %</i>	<i>at. %</i>
C4N/HCSs	9.49	8.25	90.51	91.75	/	/
C4S/HCSs	9.27	8.35	85.05	89.41	5.68	2.24
C5=S/HCSs	6.53	6.44	74.12	85.21	19.35	8.34
C4S-S/HCSs	6.09	6.68	60.40	77.25	33.51	16.07

Table S6. The pyridinic-N, pyrrolic-N, and graphite-N contents for different carbon and sulfur bonds doped carbonaceous materials based on XPS results.

Atom Percent	Pyridinic-N		Pyrrolic-N		Graphite-N	
	<i>wt. %</i>	<i>at. %</i>	<i>wt. %</i>	<i>at. %</i>	<i>wt. %</i>	<i>at. %</i>
C4N/HCSs	1.70	1.47	7.23	6.29	0.56	0.49
C4S/HCSs	3.12	2.81	5.27	4.75	0.88	0.79
C5=S/HCSs	2.57	2.54	3.28	3.23	0.68	0.67
C4S-S/HCSs	2.19	2.40	3.21	3.53	0.69	0.75

Table S7. Raman shift (cm^{-1}) and assignments for as-prepared composites

C5=S/HCSs	Assignments	C4S-S/HCSs	Assignments	C4S/HCSs	Assignments
686	C-S (ν_a)	337	S-S (ν_a)	337	S-S (ν_a)
717/716	C=S (ν_a)	462	S-S (ν_s)	462	S-S (ν_s)
738	C=S (ν_a)	686	C-S (ν_a)	686	C-S (ν_a)
842	C-S (ν_s)	842	C-S (ν_s)	842	C-S (ν_s)
893	C=S (ν_s)				
968	C=S (ν_s)				

Table S8. XPS peaks and assignments for as-prepared composites

S2 <i>p</i> (eV)	Assignments	C 1 <i>s</i> (eV)	Assignments
159.8	C-SH	284.6	C-C
160.9	C-SH	285.2	C-S
161.9	C=S	285.6	C-N
162.8	C=S	286.6	C-O
163.3	C-S	287.8	C=S
164.3	C-S	289.0	C=O
166.8	Sulfate		
168.8	Sulfate		

Table S9. Structural properties of HCSs samples

Sample	S_{BET} ($\text{m}^2 \text{g}^{-1}$)	V_{total} ($\text{cm}^3 \text{g}^{-1}$)	ρ (g cm^{-3})
C4N/HCSs	468.51	1.11	0.862
C5=S/HCSs	457.62	1.14	0.609
C4S-S/HCSs	491.23	1.47	0.508
C4S/HCSs	461.04	1.28	0.562

Table. S10. The normalization EA results of C4S-S/HCSs with different ratio of C4N/HCSs and sulfur powder (*wt./wt*)

Ratio (<i>wt./wt</i>)	S	
	<i>wt.%</i>	<i>at.%</i>
1:1	8.67	4.79
1:3	25.24	12.35
1:5	33.12	18.10
1:7	32.86	18.02

Table. S11. The normalization EA results of C4S/HCSs with different airflow velocity of Ar/H₂S-mixed atmosphere.

Airflow velocity (L min ⁻¹)	S	
	<i>wt.%</i>	<i>at.%</i>
0.03	4.25	1.78
0.05	5.78	2.28
0.10	5.82	2.31
0.20	5.75	2.45

Table. S12. The normalization EA results of C5=S/HCSs with different airflow velocity of Ar/CS₂-mixed atmosphere.

Airflow velocity (L min ⁻¹)	S	
	<i>wt.%</i>	<i>at.%</i>
0.01	15.87	7.65
0.03	23.55	10.24
0.05	23.42	10.36

Table S13. Comparison of material features and electrochemical performances between C5=S/HCSs in this work and other carbonaceous materials reported for KIBs.

Materials	Rate performance (Current density: A g ⁻¹ , Capacity: mAh g ⁻¹)								Cyclic stability	Ref.
	0.05	0.1	0.2	0.5	1.0	2.0	5.0	10.0		
C=S doped hollow carbon spheres (C5=S/HCSs)	-	-	377.9	326.2	302.5	272.7	233.0	158.4	178 mAh g⁻¹ after 4000 cycles at 2.0 A g⁻¹	This work
S/N co-doped carbon (S/NCNFAs)	-	356	260	220	198	168	112	-	168 mAh g ⁻¹ after 1000 cycles at 2.0 A g ⁻¹	8
N-doped accordion-like carbon (NALC700)	401	336	290	229	191	150	82	-	2300 cycles at 1.0 A g ⁻¹	9
N/S dual-doped porous soft carbon nanosheets (NSC)	-	325	270	241	209	160	115	-	178 mAh g ⁻¹ after 1000 cycles at 1.0 A g ⁻¹	10
carbon nanosheets (CNS)	425	362	314	267	240	215	-	-	180.2 mAh g ⁻¹ after 5000 cycles at 1 A g ⁻¹	11
N/O dual-doped porous hard carbon (NOHPHC)	-	315	-	-	-	118@3.0 A g ⁻¹	-	-	130 mAh g ⁻¹ after 1100 cycles at 1.05 A g ⁻¹	12
N/S dual-doped graphitic hollow architectures (NSG)	-	-	-	-	192	155	122	97.2	100 mAh g ⁻¹ after 5000 cycles at 5.0 A g ⁻¹	13

Carbon spheres (CS)	-	-	239.6,	213.6,	190.9	161.6	-	-	140.2 mAh g ⁻¹ after 500 cycles at 2 A g ⁻¹	14
N-doped carbon nanofibers (NCNFs-650)	-	238	217	192	172	153	126	104	164 mAh g ⁻¹ after 4000 cycles at 2 A g ⁻¹	15
S/N dual-doped hard carbon material (SNHC)	-	276	265	236	212	188	174@3.0 A g ⁻¹	-	144.9 mAh g ⁻¹ after 1200 cycles at 3A g ⁻¹	16
N/S co-doped carbon microboxes (NSC)	-	-	296.2	201.5 @0.6 A g ⁻¹	180.1	151.6	-	-	180.5 mAh g ⁻¹ at 500 mA g ⁻¹ after 1000 cycles	17
Pitch-derived soft carbon (SC-1200)	-	-	-	-	-	-	115.2	-	1000 cycles at 1.0 A g ⁻¹	18
S/O codoped porous hard carbon microspheres (S/O-PCMs)	230	213	176	158	-	-	-	-	108.4 mAh g ⁻¹ , 2000 cycles at 1.0 A g ⁻¹	19
S-doped N-rich carbon (S-NC)	-	437	369	286	234	175	114	72	141 mAh g ⁻¹ after 3000 cycles at 2.0A g ⁻¹	20
S/O-codoped Nrich 3D carbon nanoflowers (S/O-NCNFs-700)	358	297	262	226	206	-	-	-	-	21
S-doped bamboo charcoal (S-BC)	314.0	249.0	221.0	173.7	124.2	-	-	-	203.8 mAh g ⁻¹ after 300 cycles at 0.2 A g ⁻¹	22

S/N co-doping graphene nanosheets (CFM-SNG)	306.8	279.2	269.1	245	222.7	-	-	-	188.8 mAh g ⁻¹ after 2000 cycles at 1 A g ⁻¹	23
Ultrahigh N- doped carbon nanosheet (UNCN)	-	-	440@ 0.3 A g ⁻¹	330@ 0.9 A g ⁻¹	280@ 1.5 A g ⁻¹	-	230@ 3.0 A g ⁻¹	170@ 6.0 A g ⁻¹	110 mAh g ⁻¹ after 3000 cycles at 5 A g ⁻¹	24

Table S14. Comparison of material features and electrochemical performances between C5=S/HCSs in this work and other carbonaceous materials reported for SIBs.

Materials	Rate performance (Current density: A g ⁻¹ , Capacity: mAh g ⁻¹)									Cyclic stability	Ref.
	0.05	0.1	0.2	0.5	1.0	2.0	5.0	10	20		
C=S doped hollow carbon spheres (C5=S/HCSs)	-	-	343.7	307.5	284.5	257.8	224	192.2	155.8	91 mAh g ⁻¹ after 5000 cycles at 10.0 A g ⁻¹	This work
Carboxyl groups doped carbon framework (C1600-M)	382 @0.03 A g ⁻¹	-	-	-	-	152	-	-	-	141 mAh g ⁻¹ after 2000 cycles at 5 A g ⁻¹	25
N/S co-doped carbon (NSC)	-	307.2	-	237.1	206.4	186.7	178.3 @3.0 A g ⁻¹	-	-	213.6 mAh g ⁻¹ after 2000 cycles at 1 A g ⁻¹	26
Hard carbons with centralized micropores (MPC)	310	294	277	256	239	214	145	-	-	70 mAh g ⁻¹ after 5000 cycles at 5 A g ⁻¹	27
S/N codoped mesoporous hollow carbon spheres (SNMHCSs)	-	-	-	240	208	180	157	147	144	180 mAh g ⁻¹ after 7000 cycles at 20 A g ⁻¹	28
S-rich N-doped 3D porous carbon framework (SRNDC-700)	-	432.4	369.3	332.5	300	273.3	237.5	205.6	160.6	177.8 mAh g ⁻¹ 6000 cycles at 10.0 A g ⁻¹	29
Hard carbon nanofibers (HCNFs)	372-0.03	-	-	167	-	69	-	-	-	-	30
P/O co-doped Carbon materials (PO-SC-S)	249 @0.03 A g ⁻¹	229 @0.06 A g ⁻¹	211 @0.15 A g ⁻¹	187 @0.3 A g ⁻¹	170 @0.6 A g ⁻¹	145 @1.5 A g ⁻¹	125 @3.0 A g ⁻¹	-	-	-	31

S-doped N-rich carbon nanosheets (S-N/C)	350	300	280	250	220	190	150	110	-	211 mAh g ⁻¹ after 1000 cycles at 1A g ⁻¹	32
S/N co-doped carbon nanofiber (SNCNF)	-	-	-	241	212.4	190.3	153.7	121.8	-	-	33

Table S15. Comparison of material features and electrochemical performances between C5=S/HCSs in this work and other carbonaceous materials reported for LIBs.

Materials	Rate performance (Current density: A g ⁻¹ , Capacity: mAh g ⁻¹)								Cyclic stability	Ref.
	0.1	0.2	0.5	1.0	2.0	5.0	10.0	20.0		
C=S doped hollow carbon spheres (C5=S/HCSs)	-	807	660	582	507	418	319	227	326 mAh g⁻¹ after 5000 cycles at 10 A g⁻¹	This work
Pure FCC C ₆₀ nanoparticles	778	734	620	499	440	359	-	-	373 mAh g ⁻¹ after 1000 cycles at 5A g ⁻¹	34
N, P and S ternary-doped hierarchical porous soft carbon (NPSC)	668	596	500	406	305	-	-	-	489.5 mAh g ⁻¹ after 500 cycles at 0.5 A g ⁻¹	35
N-doped graphitic nanoshell (N-GNS)	553.1	504.7	464.3	433.0	387.3	294.6	-	-	372.8 mAh g ⁻¹ after 700 cycles at 1 A g ⁻¹	36
P-doped hard carbon (PHC700)	1063	-	-	-	514	432	360	-	214 mAh g ⁻¹ after 10000 cycles at 10 A g ⁻¹	37
N-doped hard carbon nanoshells (N-GCNs)	965	-	-	-	-	-	-	175	1160 mAh g ⁻¹ after 200 cycles at 0.1 A g ⁻¹	38
Pre-oxidation of hard carbon with lignin (LSHC-P200)	411	312	214	137	68	32	-	-	150 mAh g ⁻¹ after 400 cycles at 0.5 A g ⁻¹	39

Supplementary References

1. T. Yang, T. Qian, M. Wang, X. Shen, N. Xu, Z. Sun and C. Yan, *Adv. Mater.*, 2016, **28**, 539-545.
2. H. Huang, R. Xu, Y. Feng, S. Zeng, Y. Jiang, H. Wang, W. Luo and Y. Yu, *Adv. Mater.*, 2020, **32**, 1904320.
3. F. Zheng, Y. Yang and Q. Chen, *Nat. Commun.*, 2014, **5**, 5261.
4. T. Lu and F. Chen, *J. Comput. Chem.*, 2012, **33**, 580-592.
5. T. Lu and Q. Chen, *Chem.Meth.*, 2021, **1**, 231-239.
6. M. K. Y. Chan, C. Wolverton and J. P. Greeley, *J. Am. Chem. Soc.*, 2012, **134**, 14362-14374.
7. A. Urban, D.-H. Seo and G. Ceder, *npj Comput. Mater.*, 2016, **2**, 16002.
8. C. Lv, W. Xu, H. Liu, L. Zhang, S. Chen, X. Yang, X. Xu and D. Yang, *Small*, 2019, **15**, 1900816.
9. W. Zhang, M. Sun, J. Yin, K. Lu, U. Schwingenschlögl, X. Qiu and H. N. Alshareef, *Adv. Energy Mater.*, 2021, **11**, 2101928.
10. Q. Liu, F. Han, J. Zhou, Y. Li, L. Chen, F. Zhang, D. Zhou, C. Ye, J. Yang, X. Wu and J. Liu, *ACS Appl. Mater. Interfaces*, 2020, **12**, 20838-20848.
11. Y. Chen, B. Xi, M. Huang, L. Shi, S. Huang, N. Guo, D. Li, Z. Ju and S. Xiong, *Adv. Mater.*, 2022, **34**, 2108621.
12. J. Yang, Z. Ju, Y. Jiang, Z. Xing, B. Xi, J. Feng and S. Xiong, *Adv. Mater.*, 2018, **30**, 1700104.
13. C. Lu, Z. Sun, L. Yu, X. Lian, Y. Yi, J. Li, Z. Liu, S. Dou and J. Sun, *Adv. Energy Mater.*, 2020, **10**, 2001161.
14. X. Han, T. Chen, P. Zhang, Y. Qi, P. Yang, Y. Zhao, M. Shao, J. Wu, J. Weng, S. Li and F. Huo, *Adv. Funct. Mater.*, 2022, **32**, 2109672.
15. Y. Xu, C. Zhang, M. Zhou, Q. Fu, C. Zhao, M. Wu and Y. Lei, *Nat. Commun.*, 2018, **9**, 1720.
16. Y. Liu, H. Dai, L. Wu, W. Zhou, L. He, W. Wang, W. Yan, Q. Huang, L. Fu and Y. Wu, *Adv. Energy Mater.*, 2019, **9**, 1901379.
17. Y. Li, W. Zhong, C. Yang, F. Zheng, Q. Pan, Y. Liu, G. Wang, X. Xiong and M. Liu, *Chem. Eng. J.*, 2019, **358**, 1147-1154.
18. Y. Liu, Y.-X. Lu, Y.-S. Xu, Q.-S. Meng, J.-C. Gao, Y.-G. Sun, Y.-S. Hu, B.-B. Chang, C.-T. Liu and A.-M. Cao, *Adv. Mater.*, 2020, **32**, 2000505.
19. M. Chen, W. Wang, X. Liang, S. Gong, J. Liu, Q. Wang, S. Guo and H. Yang, *Adv. Energy Mater.*, 2018, **8**, 1800171.
20. L. Tao, Y. Yang, H. Wang, Y. Zheng, H. Hao, W. Song, J. Shi, M. Huang and D. Mitlin, *Energy Storage Mater.*, 2020, **27**, 212-225.
21. W. Li, D. Wang, Z. Gong, X. Guo, J. Liu, Z. Zhang and G. Li, *Carbon*, 2020, **161**, 97-107.
22. S. Tian, D. Guan, J. Lu, Y. Zhang, T. Liu, X. Zhao, C. Yang and J. Nan, *J Power Sources*, 2020, **448**, 227572.
23. W. Yang, J. Zhou, S. Wang, Z. Wang, F. Lv, W. Zhang, W. Zhang, Q. Sun and S. Guo, *ACS Energy Lett.*, 2020, **5**, 1653-1661.
24. X. Chang, X. Zhou, X. Ou, C.-S. Lee, J. Zhou and Y. Tang, *Adv. Energy Mater.*, 2019, **9**, 1902672.
25. F. Sun, H. Wang, Z. Qu, K. Wang, L. Wang, J. Gao, J. Gao, S. Liu and Y. Lu, *Adv. Energy Mater.*, 2021, **11**, 2002981.
26. J. Li, Z. Ding, L. Pan, J. Li, C. Wang and G. Wang, *Carbon*, 2021, **173**, 31-40.
27. J.-L. Xia, D. Yan, L.-P. Guo, X.-L. Dong, W.-C. Li and A.-H. Lu, *Adv. Mater.*, 2020, **32**,

- 2000447.
28. D. Ni, W. Sun, Z. Wang, Y. Bai, H. Lei, X. Lai and K. Sun, *Adv. Energy Mater.*, 2019, **9**, 1900036.
 29. B. Yin, S. Liang, D. Yu, B. Cheng, I. L. Egun, J. Lin, X. Xie, H. Shao, H. He and A. Pan, *Adv. Mater.*, 2021, **33**, 2100808.
 30. C. Cai, Y. Chen, P. Hu, T. Zhu, X. Li, Q. Yu, L. Zhou, X. Yang and L. Mai, *Small*, 2022, **18**, 2105303.
 31. F. Xie, Y. Niu, Q. Zhang, Z. Guo, Z. Hu, Q. Zhou, Z. Xu, Y. Li, R. Yan, Y. Lu, M.-M. Titirici and Y.-S. Hu, *Angew. Chem. Int. Ed.*, 2022, **61**, e202116394.
 32. J. Yang, X. Zhou, D. Wu, X. Zhao and Z. Zhou, *Adv. Mater.*, 2017, **29**, 1604108.
 33. M. Yu, Z. Yin, G. Yan, Z. Wang, H. Guo, G. Li, Y. Liu, L. Li and J. Wang, *J Power Sources*, 2020, **449**, 227514.
 34. L. Yin, J. Cho, S. J. Kim, I. Jeon, I. Jeon, M. Park, M. Park, S.-Y. Jeong, D. H. Lee, D.-H. Seo and C.-R. Cho, *Adv. Mater.*, 2021, **33**, 2104763.
 35. B. Sun, Q. Zhang, H. Xiang, F. Han, W. Tang, G. Yuan, Y. Cong, C. Fan, A. Westwood and X. Li, *Energy Storage Mater.*, 2020, **24**, 450-457.
 36. Y. J. Oh, J. H. Park, J. S. Park, S. S. Kim, S. J. Hong, Y. W. Na, J. H. Kim, S. Nam and S. J. Yang, *Energy Storage Mater.*, 2022, **44**, 416-424.
 37. Y. Qian, S. Jiang, Y. Li, Z. Yi, J. Zhou, T. Li, Y. Han, Y. Wang, J. Tian, N. Lin and Y. Qian, *Adv. Energy Mater.*, 2019, **9**, 1901676.
 38. S. Huang, Z. Li, B. Wang, J. Zhang, Z. Peng, R. Qi, J. Wang and Y. Zhao, *Adv. Funct. Mater.*, 2018, **28**, 1706294.
 39. Y.-F. Du, G.-H. Sun, Y. Li, J.-Y. Cheng, J.-P. Chen, G. Song, Q.-Q. Kong, L.-J. Xie and C.-M. Chen, *Carbon*, 2021, **178**, 243-255.